



저작자표시-비영리-변경금지 2.0 대한민국

이용자는 아래의 조건을 따르는 경우에 한하여 자유롭게

- 이 저작물을 복제, 배포, 전송, 전시, 공연 및 방송할 수 있습니다.

다음과 같은 조건을 따라야 합니다:



저작자표시. 귀하는 원저작자를 표시하여야 합니다.



비영리. 귀하는 이 저작물을 영리 목적으로 이용할 수 없습니다.



변경금지. 귀하는 이 저작물을 개작, 변형 또는 가공할 수 없습니다.

- 귀하는, 이 저작물의 재이용이나 배포의 경우, 이 저작물에 적용된 이용허락조건을 명확하게 나타내어야 합니다.
- 저작권자로부터 별도의 허가를 받으면 이러한 조건들은 적용되지 않습니다.

저작권법에 따른 이용자의 권리는 위의 내용에 의하여 영향을 받지 않습니다.

이것은 [이용허락규약\(Legal Code\)](#)을 이해하기 쉽게 요약한 것입니다.

[Disclaimer](#)

Thesis for the Degree of Master of Engineering

**Additive fabrication and characterization of
hydroxyapatite-based composite scaffolds
for bone regeneration**



by

Hoyeol Lee

Department of Industry 4.0 Convergence Bionics Engineering

The Graduate School

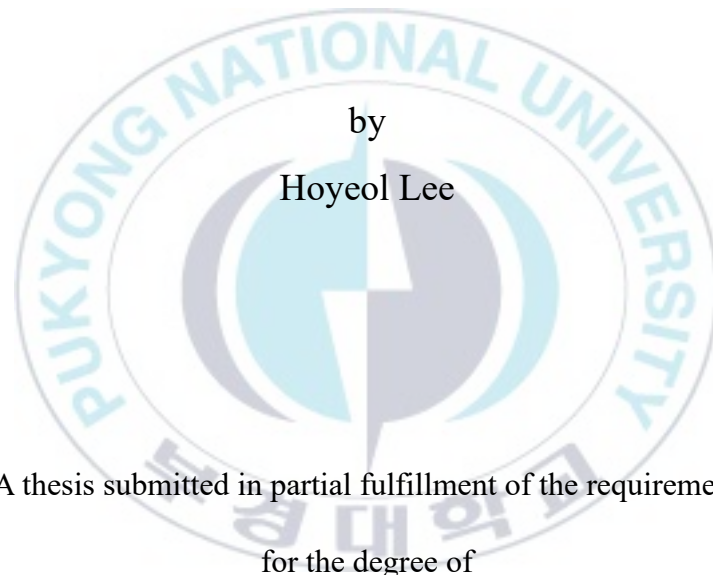
Pukyong National University

February 2022

Additive fabrication and characterization of hydroxyapatite-based composite scaffolds for bone regeneration

골재생용 수산화인회석 기반 복합
스캐폴드의 적층 제조 및 특성 분석 연구

Advisor: Prof. Seung Yun Nam



by
Hoyeol Lee

A thesis submitted in partial fulfillment of the requirement
for the degree of

Master of Engineering

in Department of Industry 4.0 Convergence Bionics Engineering,

The Graduate School,

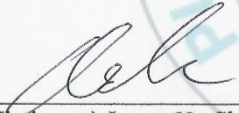
Pukyong National University

February 2022

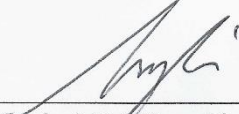
**Additive fabrication and characterization of hydroxyapatite-
based composite scaffolds for bone regeneration**

A dissertation
by
Hoyeol Lee

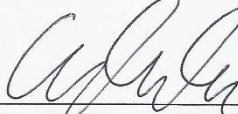
Approved by:



(Chairman) Joong Ho Shin



(Member) Hae Gyun Lim



(Member) Seung Yun Nam

February 25, 2022

골재생용 수산화인회석 기반 복합 스캐폴드의 적층 제조 및 특성 분석 연구

이 호 열

부경대학교 대학원 4 차산업융합바이오닉스공학과

요 약

세계적인 인구 고령화에 의한 골 결손 질환 유병률의 꾸준한 증가로 효과적인 치료를 위한 골 이식 대체제 개발연구가 활발히 진행되고 있다. 특히, 3D 프린팅 기술을 이용하여 생체재료를 적층 가공한 조직공학용 스캐폴드는 의료 영상을 기반으로 환자 맞춤형 치료가 가능하다는 장점에 의해 기존 골 이식제의 대체제로서 각광을 받고 있다. 하지만 스캐폴드를 제작함에 있어 안정적인 적층을 위한 우수한 인쇄적성과 세포친화적인 환경제공을 위한 생체모방성을 동시에 만족하는 생체재료가 없어 이상적인 골 재생을 위한 재료개발 연구가 필요한 실정이다. 따라서, 본 연구에서는 뼈 무기물의 주성분으로서 골 재생연구에 널리 적용되고 있는 수산화인회석을 기반으로 생체모방 복합 스캐폴드를 3D 프린팅을 이용해 제작하였다. 또한, 제작한 복합 스캐폴드의 인쇄적성, 이화학적 특성, 기계적 특성 및 골 분해능력 등을 분석하여 성능을 평가함으로써 기존 골 이식제를 대체할 수 있는 효과적인 대안을 제시하였다.

Table of contents

Abstract	i
Table of contents	ii
List of tables	v
List of figures	vi
1. Introduction	1
2. Characterization of 3D-printed biomimetic bone scaffolds with high HA content	5
2.1. Materials and methods	7
2.1.1. Preparation of HA/gelatin composites	7
2.1.2. Rheological characterization	7
2.1.3. Fabrication of composite scaffolds	8
2.1.4. Physicochemical and structural characterization	8
2.1.5. Mechanical characterization	9
2.1.6. Biological characterization	9
2.2. Results and discussion	10
2.2.1. Rheological properties of HA/gelatin composites	10

2.2.2. Fabrication of HA/gelatin composite scaffolds -----	12
2.2.3. Chemical and structural properties of HA/gelatin composite scaffolds -----	14
2.2.4. Mechanical properties of HA/gelatin composite scaffolds -----	17
2.2.5. Biological properties of HA/gelatin composite scaffolds -----	18
3. Optimized fabrication and characterization of 3D-printed bone scaffolds based on HA/gelatin composites reinforced with graphene oxide (GO) --	21
3.1. Materials and methods -----	25
3.1.1. Materials -----	25
3.1.2. The synthesis of graphene oxide -----	25
3.1.3. Preparation of the HA/gelatin/GO composites -----	26
3.1.4. Characterization of HA powder, GO, and the HA/gelatin/GO composites -----	27
3.1.5. Rheological measurements of the HA/gelatin/GO composites -	27
3.1.6. 3D-printing of HA/gelatin/GO scaffold -----	28
3.1.7. Morphological and mechanical characterization of HA/gelatin/GO scaffolds -----	29
3.1.8. Statistical analysis -----	31

3.2. Results and discussion	31
3.2.1. The mechanical properties of the HA/Gelatin/GO scaffolds fabricated via the conventional method	31
3.2.2. Characterization of HA powder, GO, and the HA/gelatin/GO composites	34
3.2.3. Rheological and printability assessments of the HA/gelatin/GO composites	37
3.2.4. The structural and morphological properties of 3D-printed HA/gelatin/GO composite scaffolds	42
3.2.5. The mechanical properties of 3D-printed HA/gelatin/GO composite scaffolds	43
4. Conclusions	46
5. References	48

List of tables

Table 1. HA content of four HA/gelatin composites ----- 7

Table 2. Concentrations of the components in the HA/gelatin/GO composites -
----- 26



List of figures

- Figure 1.** Rheological properties of HA/gelatin composites with different amounts of HA. (a) Shear storage and loss moduli as a function of temperature. (b) Complex viscosity as a function of angular frequency at 20 °C -----
----- 11
- Figure 2.** Printability assessment of HA/gelatin composites with different amounts of HA. Microscopic images (scale bar = 500 μm) and photographs (scale bar = 5 mm) of 3D-printed HA/gelatin composite scaffolds with (a,e) 0%, (b,f) 60%, (c,g) 70%, and (d,h) 80% HA. Statistical analysis of (i) strut diameters and (j) pore sizes. Photographs of 60% HA/gelatin composite scaffold under optimal printing conditions: (k) top and (l) side view (scale bar = 5 mm) -----
----- 13
- Figure 3.** (a) TEM image of HA powder (scale bar = 100 nm). (b) FTIR, (c) XRD, and (d) wide-scan XPS spectra of HA/gelatin composites (0%, 60%, 70%, and 80% HA) and HA powder ----- 16
- Figure 4.** SEM images (scale bar = 500 μm) of HA/gelatin composite scaffolds with (a,d) 60%, (b,e) 70%, and (c,f) 80% HA contents. The insets show high-magnification (500 \times) images of the surface of the scaffold. (a–c) Top views; (d–f) side views ----- 17

Figure 5. (a) Representative stress-strain curves and (b) compressive strengths of HA/gelatin composite scaffolds	18
Figure 6. (a) Cell proliferation and (b) fluorescence microscopy images (scale bar = 500 μ m) of Hoechst-stained ADMSCs attached on HA/gelatin composite scaffolds	20
Figure 7. (a) ALP activity and (b) ARS absorbance of ADMSCs incubated on HA/gelatin composite scaffolds	20
Figure 8. A schematic of the fabrication process for the 3D-printing of HA/Gelatin/GO composite scaffolds	29
Figure 9. Compressive strength testing of conventionally fabricated HA/gelatin/GO composite cylindrical scaffolds. (a) Representative images of the fabricated HA/gelatin/GO specimens used in the compressive strength testing (scale bar = 2 mm). Stress-strain curves of HA/gelatin/GO specimens fabricated with various GO concentrations of (b) 0%, (c) 0.5%, and (d) 1%. (e) Compressive strength bar charts of the fabricated HA/gelatin/GO specimens. (f) Young's modulus plots of the fabricated HA/gelatin/GO specimens. The effect of varying the degree of GO reinforcement of HA/gelatin specimens on (g) compressive strength and (h) Young's modulus	33

Figure 10. (a) A transmission electron microscopy (TEM) image of graphene oxide (GO), and (b) UV-Vis absorption spectra and (c) wide-scan X-ray photoelectron spectroscopy (XPS) spectra of GO and graphite ----- 34

Figure 11. Characterization of HA powder, GO, and HA/gelatin/GO composites. (a) XRD patterns, (b) FTIR spectra, (c) Raman spectra, and (d) TGA curves ----- 37

Figure 12. Rheological and printability assessments of the HA/gelatin/GO composites. (a) Oscillatory frequency sweep testing, (b) complex viscosity as a function of angular frequency, (c) oscillatory temperature ramp testing, (d) extrudability at various printing temperatures, and (e) flow rate at various extrusion pressure levels with the optimized printing temperature. (f) Representative images of the 3D-printed HA/gelatin/GO scaffolds at various printing velocities at the optimized printing temperature (scale bar = 5 mm). The inset frames are microscopy images of the 3D-printed scaffolds (scale bar = 500 μm). (g and h) Quantitatively analyzed strut diameters of the 3D-printed HA/gelatin/GO scaffolds ----- 41

Figure 13. Morphological analysis of 3D-printed HA/gelatin/GO scaffolds. (a–c, g–i) Photographs (scale bar = 5 mm) and (d–f, j–l) SEM images (scale bar = 500 μm) ----- 42

Figure 14. Compressive and flexural properties of 3D-printed HA/gelatin/GO scaffolds. (a) Stress-strain curves, (b) the testing platform for the compressive testing, (c) compressive strength, and (d) Young's modulus plots of the specimens. (e) Weibull plots to establish the flexural strengths, (f) the testing platform for the flexural testing (g) flexural strength of the specimens, and (h) Weibull modulus, characteristic strength, and correlation coefficient values of the 3D-printed scaffolds ----- 45



1. Introduction

The aging global population has resulted in an increased incidence of bone defects following trauma or diseases in recent years [1-3]. For instance, the most common type of bone disease, osteoporosis, is estimated to affect more than 200 million people worldwide [4]. However, critical-sized bone defects cannot be completely healed by the self-healing ability of the human body [5, 6]. Hence, more than two million of bone graft implantations are performed annually around the world [7]. However, conventional bone grafts, including autografts and allografts, suffer from various drawbacks, such as limited availability and donor site morbidity [8-10]. To overcome these shortcomings, tissue-engineered bone substitutes prepared using a combination of novel biomaterial and fabrication techniques have emerged as a promising therapeutic alternative [6]. Among the various techniques used to fabricate tissue-engineered bone constructs, three-dimensional (3D) bioprinting has been widely explored as an effective alternative, which provides cell-friendly microenvironments with a designed shape and porosity that promote bone repair and regeneration [11, 12]. The flexibility associated with the fabrication of tissue-engineered scaffolds customized via computer-aided design and medical imaging can be advantageous for personalized bone defect treatments [13]. However, 3D-bioprinted bone substitutes are still affected by significant issues, such as the limited availability of printable biomaterials that meet key requirements, including excellent printability, high mechanical integrity, low toxicity, and appropriate cell interactions [14]. Therefore, these limitations present a significant challenge to the robust and accurate fabrication

of bioprinted bone scaffolds capable of promoting effective regeneration of the target tissues [15, 16]. For instance, the thermoplastic behavior and relatively low melting point of polycaprolactone (PCL), an FDA-approved biodegradable synthetic polymer, enables its easy processing into bone scaffolds fabricated with extrusion-based 3D bioprinting techniques. However, despite the biocompatibility and ease of fabrication of PCL, its intrinsic hydrophobicity and lack of osteoinductivity inhibit cell attachment and osteogenic differentiation, frequently preventing successful therapy [17, 18].

To overcome the limitations of homogeneous material-based scaffolds in bone tissue engineering, several studies have investigated the use of bioceramic/polymer composites to improve the mechanical and biological properties of bone grafts [19, 20]. The primary advantage of these materials is their biomimetic composition, which efficiently mimics the natural inorganic and organic constituents of bone tissue [21]. Bioceramics, such as hydroxyapatite (HA), tricalcium phosphate (TCP), and bioactive glasses, have been commonly used in bioceramic/polymer composites due to their similarity with the mineral phase of the natural bone matrix [22]. Among bioceramics for bone tissue-engineered scaffolds, HA is one of the most extensively studied materials due to its excellent physicochemical properties, such as osteoconductivity, bioactivity, and resorbability, which can compensate the limitations of polymeric matrices [16, 21, 23]. The addition of HA to a polymer improves not only the osteogenic properties of the fabricated composite scaffold but also its rheological properties, enhancing both mechanical strength and shape fidelity [19].

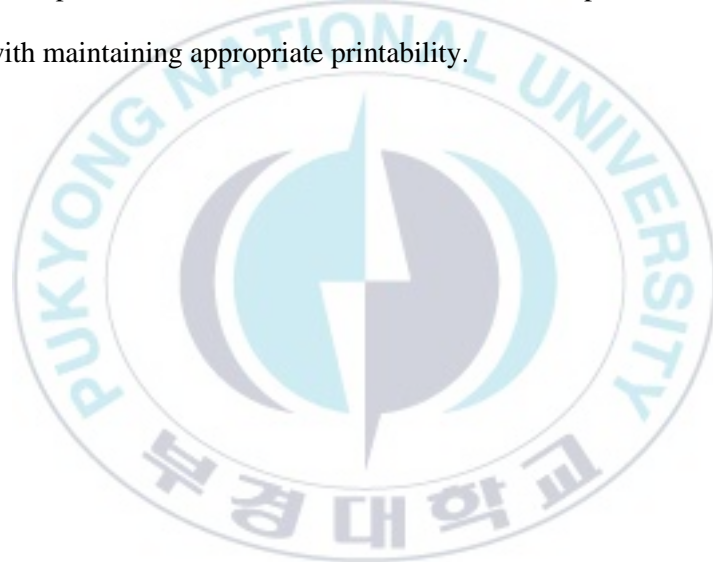
Both biocompatible synthetic polymers, such as polylactic acid (PLA), polylactic-co-glycolic acid (PLGA), and PCL, and natural hydrogels, such as collagen, alginate,

and gelatin, have been widely used as the organic component of bioceramic/polymer composites for bone tissue engineering applications [21]. However, the inherent limitations of synthetic polymers, such as lack of bioactivity and relatively high viscosity, can negatively affect the desired microenvironment for effective cellular interactions and the bioceramic contents ($\leq 50\%$) [24]. In contrast, natural hydrogels can induce bioactive responses through the biofunctional molecules absorbed on their surface, which can enhance cell attachment, proliferation, and differentiation [16]. Moreover, natural hydrogels are frequently used for 3D bioprinting due to their shear-thinning properties and excellent bioactivity, but their poor mechanical properties can significantly limit effective bone repair in preclinical and clinical models [25, 26]. Hence, several studies have attempted to improve the crosslinking and geometrical features of hydrogels to enhance the efficacy of bone defect treatments using bioprinted hydrogels [27, 28].

To overcome the above limitations, multiple combinations of bioceramic/hydrogel composites, including α -TCP/gelatin, HA/alginate, and bioactive glass/gelatin, have been explored for bone tissue regeneration [19, 21]. Although many studies have been performed on bioceramic/hydrogel composites, the fabricated composite scaffolds are mechanically and compositionally not compatible with natural bone due to the intrinsic limitations of hydrogels and the low bioceramic contents. Furthermore, bioprinting of composites with high bioceramic contents is challenging because of their high rheological resistance; hence, these materials are seldom employed in bioprinting. Therefore, this thesis aims at discussing and analyzing new approaches for high contents HA-based hydrogel composite as 3D printing (also known as additive

fabrication) applications toward bone tissue regeneration. Two 3D printing approaches are employed to improve the applicability and functionality of HA as a printing material.

Firstly, in chapter 2, gelatin-based composites incorporating large weight fractions ($\geq 60\%$) of nanosized HA were used to provide an adequate biomimetic environment for bone tissue regeneration, with compositional and mechanical similarity to the natural bone matrix. Secondly, in chapter 3, graphene oxide (GO) reinforced HA/gelatin composite scaffolds were demonstrated to improve their mechanical properties with maintaining appropriate printability.



2. Characterization of 3D-printed biomimetic bone scaffolds with high HA content

With the increased incidence of bone defects following trauma or diseases in recent years, three-dimensional porous scaffolds fabricated using bioprinting technologies have been widely explored as effective alternatives to conventional bone grafts, which provide cell-friendly microenvironments promoting bone repair and regeneration. However, the limited use of biomaterials poses a significant challenge to the robust and accurate fabrication of bioprinted bone scaffolds that enable the effective regeneration of the target tissues. Although bioceramic/polymer composites can provide tunable biomimetic conditions, their effects on the bioprinting process are unclear. Thus, in this study, we fabricated hydroxyapatite (HA)/gelatin composite scaffolds containing large weight fractions of HA using extrusion-based bioprinting, with the aim to provide an adequate biomimetic environment for bone tissue regeneration with compositional and mechanical similarity to the natural bone matrix. The overall features of the bioprinted HA/gelatin composite scaffolds, including rheological, morphological, physicochemical, mechanical, and biological properties, were quantitatively assessed to determine the optimal conditions for both fabrication and therapeutic efficiency. The present results show that the bioprinted bioceramic/hydrogel scaffolds possess excellent shape fidelity; mechanical strength comparable to that of native bone; and enhanced bioactivity in terms of cell proliferation, attachment, and osteogenic

differentiation. This study provides a suitable alternative direction for the fabrication of bioceramic/hydrogel-based scaffolds for bone repair based on bioprinting.



*This work has been published as "Additive Fabrication and Characterization of Biomimetic Composite Bone Scaffolds with High Hydroxyapatite Content". *Gels*. 2021;7(3):100.

2.1. Materials and methods

2.1.1. Preparation of the HA/gelatin composites

Nano-sized hydroxyapatite powder (< 200 nm particle size, nGimat) and type A gelatin (porcine skin, Sigma Aldrich) were used to fabricate HA/gelatin composites. Gelatin powder was dissolved in distilled water on a rotational shaker at 50 °C and mixed with either 4.5, 7, or 12 g of HA powder (Table 1). The mixture was placed in a planetary centrifugal mixer (AR-100, Thinky) for 1-2 minutes to make homogeneous HA/gelatin composites.

Table 1. HA content of four HA/gelatin composites.

Sample	HA content (wt%)	HA (g)	Gelatin (g)	Distilled water (mL)
1	0	0	3	15
2	60	4.5	3	15
3	70	7	3	15
4	80	12	3	15

2.1.2. Rheological characterization

Rheological measurements of HA/gelatin composites were performed with a rheometer (HR-2, TA instruments) operating in the oscillatory mode using a 20 mm parallel plate with a 500 μ m gap. The amplitude sweep test was performed at 1 Hz to confirm the linear viscoelastic region before other rheological measurements. For the temperature sweep test, -5 °C/min temperature ramps were conducted from 40 °C to 10 °C at a 1 Hz frequency and 1% strain. For the frequency sweep test, the angular frequency was increased from 0.1 to 100 rad/s at 20 °C with a 1% strain.

2.1.3. Fabrication of composite scaffolds

The HA/gelatin composite scaffolds were fabricated with a self-developed 3D bioprinting system. The nozzle temperature was set between 30 and 50 °C, according to the contents of each HA/gelatin composite. The printing velocity and extrusion pressure ranges were 5–15 mm/s and 200–400 kPa, respectively. The porous structure was generated in a 0°/90° orientation with a nozzle diameter of 0.51 mm. The distance between printed fibers was set to 1 mm for biological characterizations and 1.4 mm for the other measurements. The external dimensions of the scaffolds were set to 19.6 × 19.6 mm. The strut diameter and pore size of the printed scaffolds were quantified by optical image processing using the MATLAB software.

After fabrication, the scaffolds were immersed in a 0.25% w/v solution of glutaraldehyde for 10 min at room temperature to chemically crosslink the gelatin polymeric chains. To remove the remaining glutaraldehyde, the scaffolds were washed three times with distilled water.

2.1.4. Physicochemical and structural characterization

The chemical structure and composition of the HA powder and fabricated HA/gelatin composite scaffolds were analyzed by XRD (X'Pert-MPD, Philips, Eindhoven, The Netherlands), FTIR spectroscopy (FT-4100, Jasco, Tokyo, Japan), and XPS (AXIS Supra, Kratos, UK). The morphologies of the HA powder and HA/gelatin composite scaffolds were inspected by field-emission TEM (JEM-F200, JEOL, Tokyo, Japan) and low-vacuum SEM (JSM-6490LV, JEOL, Tokyo, Japan).

2.1.5. Mechanical characterization

To assess their mechanical properties, the composite scaffolds were cut into small pieces ($5.6 \times 5.6 \times 6$ mm; 12 layers) and dried at $37\text{ }^{\circ}\text{C}$ overnight. A compressive test was then conducted with a universal testing machine (LR5K Plus, Lloyd Instruments, Bognor Regis, UK) at a constant cross-head speed of 1 mm/min. Five samples of each scaffold were tested to ensure the reliability of the results.

2.1.6. Biological characterization

Rat adipose-derived mesenchymal stem cells (RASMD-01001, Cyagen, Santa Clara, USA) were used to evaluate the cellular behavior on the scaffolds. The fabricated scaffolds were prepared with six layers and cut to $5.6 \times 5.6 \times 3$ mm pieces, then sterilized with ethanol and ultraviolet (UV) light. The cells (3×10^4 cells/scaffold) were seeded on each scaffold and cultivated in Dulbecco's modified Eagle's medium (DMEM) supplemented with 10% fetal bovine serum (FBS), 1% penicillin–streptomycin (pen–strep), and 1% non-essential amino acids. The seeded scaffolds were incubated at $37\text{ }^{\circ}\text{C}$ with 5% CO_2 . Before seeding the cells, the scaffolds were preincubated in a culture medium for 24 h. The cells from the fifth passage were used in all experiments.

After 1 and 3 days of culturing on scaffolds, cell viability was evaluated using the MTT assay. The cell-seeded scaffolds were treated with 0.5 mg/mL MTT solution for 4 h at $37\text{ }^{\circ}\text{C}$. The scaffolds were then placed in dimethylsulfoxide (DMSO) for 30 min at room temperature to dissolve the MTT formazan. The solubilized formazan was measured in a microplate reader (Epoch, BioTek, Winooski, VT, USA) at 540 nm. Each time point was tested in triplicate. After 4 days of cell culture, cell attachment on the

scaffold was evaluated by Hoechst 33,342 staining and fluorescent microscopy imaging (Eclipse Ts2, Nikon, Tokyo, Japan).

ALP assay and ARS tests were performed to analyze the osteogenic differentiation of ADMSCs on the scaffolds. The cells were seeded as described above, incubated for 24 h, and transferred to osteogenic differentiation media consisting of DMEM supplemented with 10% FBS, 1% pen-strep, 50 µg/mL l-ascorbic acid, 10 mM β-glycerophosphate, 10 nM calcitriol, and 100 nM dexamethasone. After 14 days, the osteogenic activity was assessed by ALP assay. The scaffolds were washed with PBS and gently submerged in 1-step p-nitrophenyl phosphate (pNPP) solution; then, the absorbance was measured at a wavelength of 405 nm using a microplate reader.

Calcium mineralization was evaluated by ARS staining. After incubating them for 21 days, the scaffolds were washed with PBS and fixed with 70% cold ethanol at room temperature for 1 h. Then, the ethanol-fixed scaffolds were stained with ARS (pH 4.2) for 20 min. To quantify calcium mineralization, the scaffolds were incubated in 10 mM sodium phosphate buffer (pH 7.0) containing 10% cetylpyridinium chloride for 15 min, and the absorbance was measured at a wavelength of 562 nm. Three samples were tested for each incubation time.

2.2. Result and discussion

2.2.1. Rheological properties of HA/gelatin composites

In 3D bioprinting applications, rheological properties are known to be significantly correlated with printing accuracy and shape fidelity [29-31]. Therefore, the rheological characteristics of HA/gelatin composites were investigated to predict the deposition

quality and optimize the printing parameters before the additive fabrication of the composite bone scaffolds [32-34]. The influence of the temperature on the rheological properties of the HA/gelatin composites was assessed at four different concentrations of HA (0%, 60%, 70%, and 80%). Each group in Fig. 1(a) exhibits a change in storage modulus (G') and loss modulus (G'') as the temperature varied from 10 to 40 °C. While the G' and G'' curves of gelatin alone (without HA) crossed near 30 °C, indicating the sol–gel transition, the G' values of HA/gelatin samples were higher than the G'' values, and the corresponding curves in each group did not cross, reflecting the enhanced mechanical stability of the hydrogel upon the addition of the bioceramic. Overall, the G' and G'' values increased with increasing HA contents from 0 to 80%. The complex viscosities (η^*) of the HA/gelatin composites were also measured at 20 °C with varying angular frequencies (ω), as shown in Fig. 1(b). The viscosity of the HA/gelatin composite increased with the amount of HA. In addition, all viscosity curves exhibited distinct shear-thinning behaviors without any plateau.

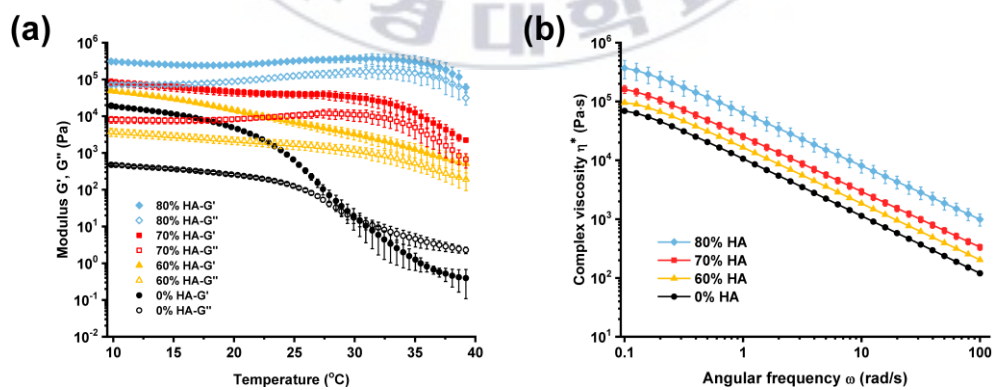


Figure 1. Rheological properties of HA/gelatin composites with different amounts of HA. (a) Shear storage and loss moduli as a function of temperature. (b) Complex viscosity as a function of angular frequency at 20 °C.

2.2.2. Fabrication of HA/Gelatin composite scaffolds

To evaluate the printability of each HA/gelatin composite, three-layered HA/gelatin composite scaffolds were initially fabricated with HA contents of 0%, 60%, 70%, and 80%, based on the rheological properties of each group (Fig. 2(a–h)). In the case of 0% HA, gelatin showed significantly poor printability at both lower and higher temperatures than the sol–gel transition temperature (near 30 °C) due to its low shear moduli and over-gelation [35]. However, due to the increased shear moduli and viscosities upon the addition of HA, the HA/gelatin composites could be additively fabricated with excellent printability using an extrusion-based bioprinting technique. The strut diameter and pore size of the printed scaffolds were then analyzed to quantify their printing accuracy. The calculated strut diameter and pore size of the scaffolds with 60%, 70%, and 80% HA were similar to each other and comparable to ideal printing conditions (strut diameter: 510 μm ; pore size: 890 μm). However, the scaffold prepared without HA exhibited a significantly inconsistent strut diameter and pore size, which were substantially different from the nozzle diameter and pore size of the initially designed structure (Fig. 2(i) and 2(j)). These experimental results indicate that the incorporation of bioceramics such as HA into hydrogels can enhance their extrudability and printing accuracy, which is essential for the additive fabrication of tissue-engineered constructs [36]. In addition, the enhanced rheological properties enabled the HA/gelatin composite to be deposited in 12 layers with high shape fidelity (Fig. 2(k) and 2(l)).

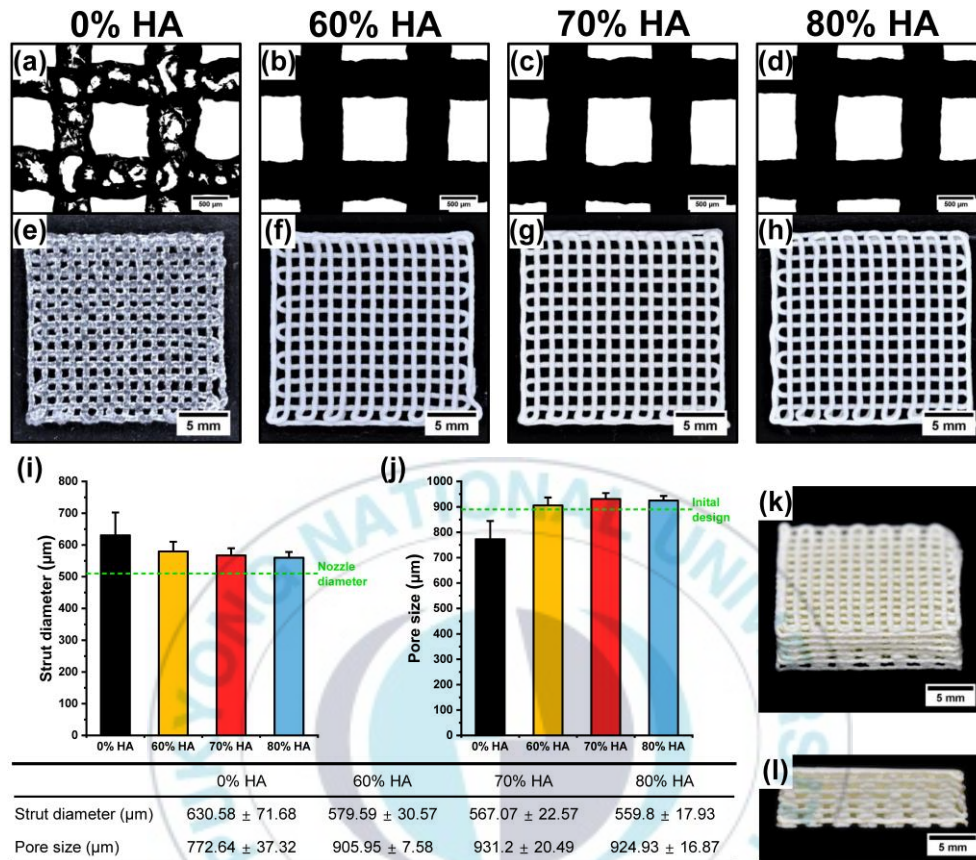


Figure 2. Printability assessment of HA/gelatin composites with different amounts of HA. Microscopic images (scale bar = 500 μm) and photographs (scale bar = 5 mm) of 3D-printed HA/gelatin composite scaffolds with (a,e) 0%, (b,f) 60%, (c,g) 70%, and (d,h) 80% HA. Statistical analysis of (i) strut diameters and (j) pore sizes.

Photographs of 60% HA/gelatin composite scaffold under optimal printing conditions: (k) top and (l) side view (scale bar = 5 mm).

2.2.3. Chemical and Structural Properties of HA/Gelatin Composite

Scaffolds

The morphology of HA powders was investigated by transmission electron microscopy (TEM), as shown in Fig. 3(a). The TEM images indicated the presence of spherical-shaped HA nanoparticles. The chemical structure of the HA/gelatin composite scaffolds was investigated using FTIR, XRD, and XPS. The FTIR spectra of all fabricated scaffolds display a series of amide and carboxyl bands corresponding to the chemical structure of gelatin (Fig. 3(b)). The peaks at 1644, 1536, and 1239 cm^{-1} were attributed to the C=O stretching (amide I), N–H bending (amide II), and N–H stretching (amide III) vibrations, respectively [37], while the peak at 1450 cm^{-1} was associated with carboxyl groups [38]. For effective analysis of the HA vibrational properties, the FTIR spectrum of pure HA powder was also measured and compared with those of the scaffolds. According to this analysis, the peaks at 603 and 575 cm^{-1} were attributed to the bending vibration of the phosphate group, while those at 1059, 1093, and 963 cm^{-1} were associated with the phosphate stretching vibration [39]. All fabricated scaffolds, except the HA-free gelatin scaffold, showed the characteristic peaks of the phosphate group, whose intensity increased slightly with the HA content. The physical structures of the HA powder and fabricated HA/gelatin composite scaffolds were assessed using XRD (Fig. 3(c)). Only the scaffold without HA showed a large amorphous hump around $2\theta = 20^\circ$, which is the typical XRD pattern of pure gelatin, originating from its α -helix and triple-helical structure [40]. Distinct peaks were observed in the XRD patterns of the pure HA powder at 2θ values of 25.99° corresponding to the (002) reflection; 28.43° for reflections (102) and (210); 31.9°

(triplet) for reflections (211), (112), and (300); and 34° for reflection (202). These are the principal diffraction peaks of HA, according to the JCPDS card no. 09-0432 [37]. Apart from the HA-free scaffold, all fabricated scaffolds containing HA exhibited distinct characteristic HA peaks.

The elemental compositions of the HA powder and fabricated HA/gelatin composite scaffolds were analyzed using XPS. As shown in Fig. 3(d), the spectra of all fabricated scaffolds incorporating HA showed the characteristic peaks of HA at 133, 199, 347, and 437 eV, attributed to P 2p, P 2s, Ca 2p, and Ca 2s states, respectively [41]. Furthermore, the intensity of these peaks increased with the HA content. The N 1s peak at 400 eV, indicating the presence of gelatin, was observed in the spectra of all scaffolds [42].

The morphology and architecture of composite scaffolds containing HA were visualized using SEM (Fig. 4). The scaffold pores were completely open and matched well with the predesigned structure of all three scaffolds. The composite scaffold with high HA content showed a relatively smooth surface compared to those with lower HA contents, at both low and high magnification. The roughness of the scaffold surface was strongly dependent on the HA and gelatin contents, which may be due to the influence of the degree of evaporation during the drying process [43].

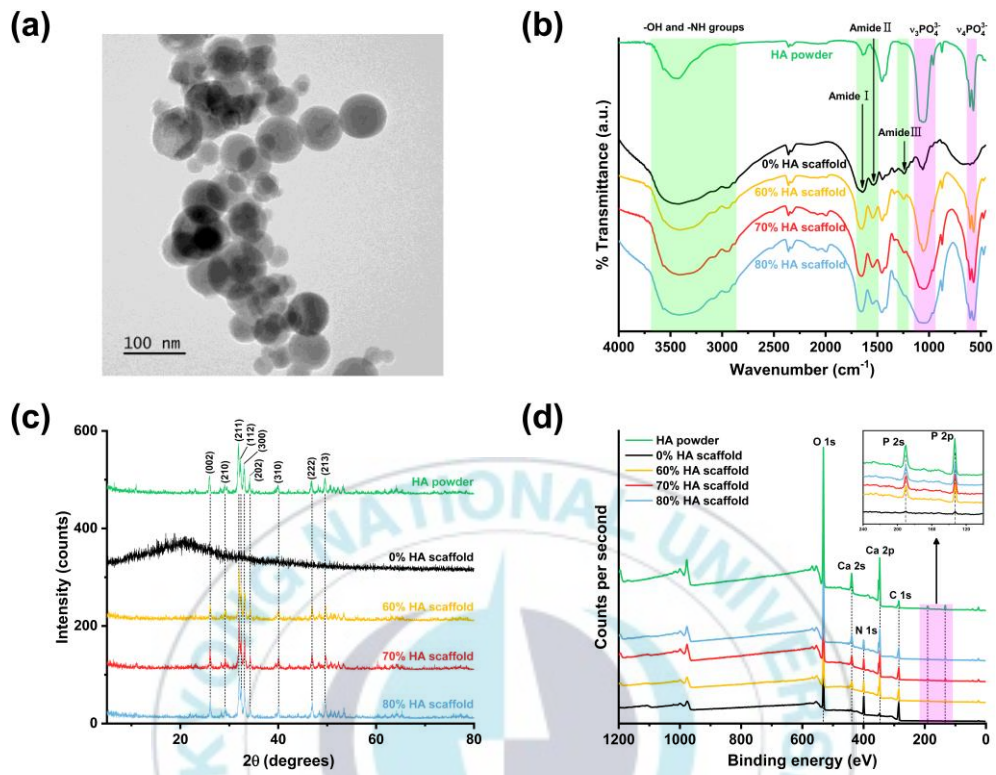


Figure 3. (a) TEM image of HA powder (scale bar = 100 nm). (b) FTIR, (c) XRD, and (d) wide-scan XPS spectra of HA/gelatin composites (0%, 60%, 70%, and 80% HA) and HA powder.

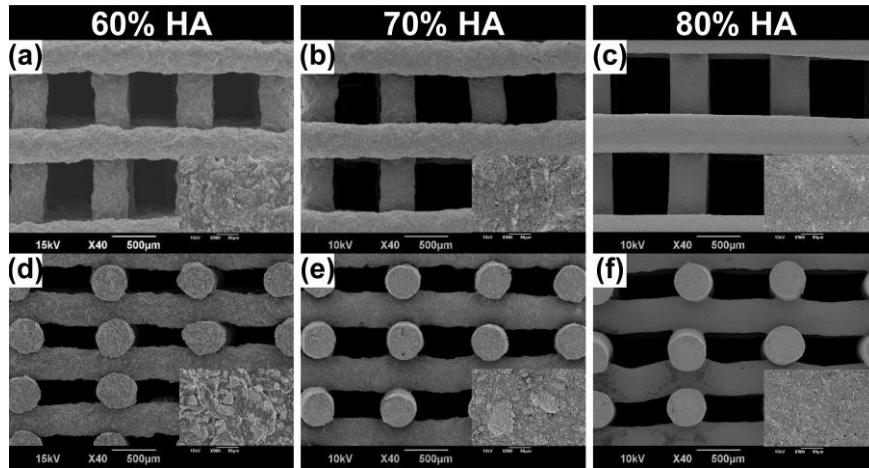


Figure 4. SEM images (scale bar = 500 μm) of HA/gelatin composite scaffolds with (a,d) 60%, (b,e) 70%, and (c,f) 80% HA contents. The insets show high-magnification (500 \times) images of the surface of the scaffold. (a–c) Top views; (d–f) side views. 3. (a) TEM image of HA powder (scale bar = 100 nm). (b) FTIR, (c) XRD, and (d) wide-scan XPS spectra of HA/gelatin composites (0%, 60%, 70%, and 80% HA) and HA powder.

2.2.4. Mechanical Properties of HA/Gelatin Composite Scaffolds

To quantitatively assess the role of HA on the mechanical properties of the HA/gelatin composite scaffold, compressive tests were performed with varying concentrations of HA, as shown in Fig. 5(a). The strain values at the maximum applied stress decreased with increasing contents of HA (approximately 7% for 60% HA, 5% for 70% HA, and 3% for 80% HA), indicating that the composite scaffolds became less ductile due to the interference of the bioceramic with the hydrogel crosslinking. The highest compressive strengths observed for 60%, 70%, and 80% HA contents were 2.3 ± 0.4 , 8.4 ± 2.7 , and 4.1 ± 0.8 MPa, respectively (Fig. 5(b)). Moreover, the compressive strengths of all HA/gelatin scaffolds were comparable to that of cancellous bone [44,

45]. The 70% HA scaffold, with a similar composition to native bone, had a significantly higher compressive strength compared to the other samples. These results confirm the feasibility of using bioprinted bone scaffolds to mimic the mechanical properties and composition of native bone tissue, overcoming the limitations of current bioceramic/polymer composite scaffolds [46-48].

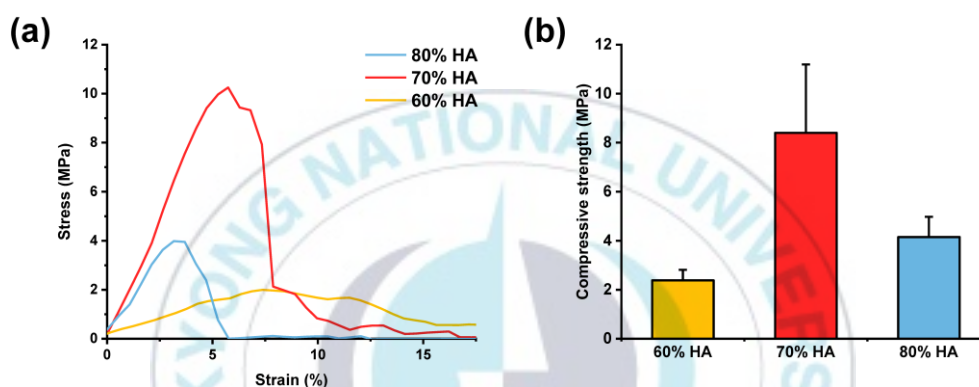


Figure 5. (a) Representative stress–strain curves and (b) compressive strengths of HA/gelatin composite scaffolds.

2.2.5. Biological Properties of HA/Gelatin Composite Scaffolds

To assess the effect of the HA/gelatin composite scaffolds on cell proliferation and attachment, ADMSCs were cultured on the scaffolds. The cell proliferation in each scaffold was evaluated at days 1 and 3 using the 3-(4,5-dimethylthiazol-2-yl)-2,5-diphenyltetrazolium bromide (MTT) assay (Fig. 6(a)). At both time points, all scaffolds containing HA showed higher absorbance values than those without HA. The highest cell proliferation was observed for the scaffold containing 60% HA, as indicated by a significantly higher absorbance value than that of the other three groups. These data

imply that the presence of HA in the scaffolds can stimulate the proliferative response of ADMSCs.

To assess the cell attachment, we obtained fluorescence images of Hoechst-stained mesenchymal stem cells attached on the scaffolds (Fig. 6(b)). Similar to the MTT results, the highest number of proliferated cells was detected on the surface of the scaffold with 60% HA. However, a relatively low number of cells were observed in the 80% HA scaffold compared to the others. The reduced cell attachment to this scaffold might be due to its relatively smooth surface (as shown in Fig. 4) and reduced accessibility of cell-binding motifs owing to the relatively low gelatin proportion [49].

Many studies have demonstrated that the surface properties of a scaffold can affect cell attachment, proliferation, differentiation, and even morphology [50-52]. It is well known that the gelatin used in scaffolds can facilitate the exposure of cell-binding motifs (i.e., RGD) that enable biological interactions between cells and scaffolds [19]. Moreover, the introduction of hydroxyapatite alters the microscale surface roughness of the scaffold, which, in turn, can affect its cellular response, enhancing cell attachment and proliferation [51]. Therefore, the appropriate proportions of HA and gelatin must be adopted in the composite scaffolds to achieve the effective bone repair.

The osteogenic differentiation of ADMSCs was assessed by evaluating the alkaline phosphatase (ALP) activity and calcium deposition by alizarin red S (ARS) staining. The HA-containing scaffolds had a higher ALP activity than those without HA at day 14 (Fig. 7(a)). Furthermore, the scaffolds with 60–80% HA had higher ARS absorbance values than the 0% HA scaffold at day 21 (Fig. 7(b)). These results imply that the HA particles incorporated in the scaffolds can promote the osteogenic differentiation of

ADMSCs, likely by enhancing the ALP activity of mesenchymal stem cells and stimulating the endogenous expression of osteogenic growth factors, such as bone morphogenetic proteins [16].

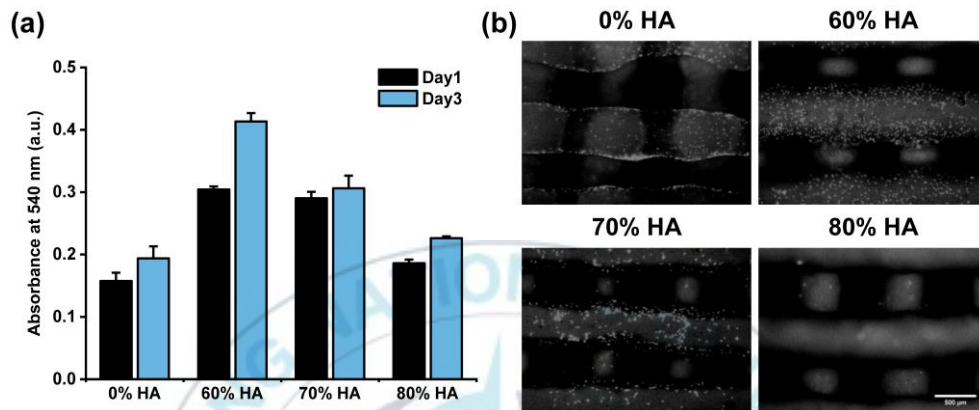


Figure 6. (a) Cell proliferation and (b) fluorescence microscopy images (scale bar= 500 μm) of Hoechst-stained ADMSCs attached on HA/gelatin composite scaffolds.

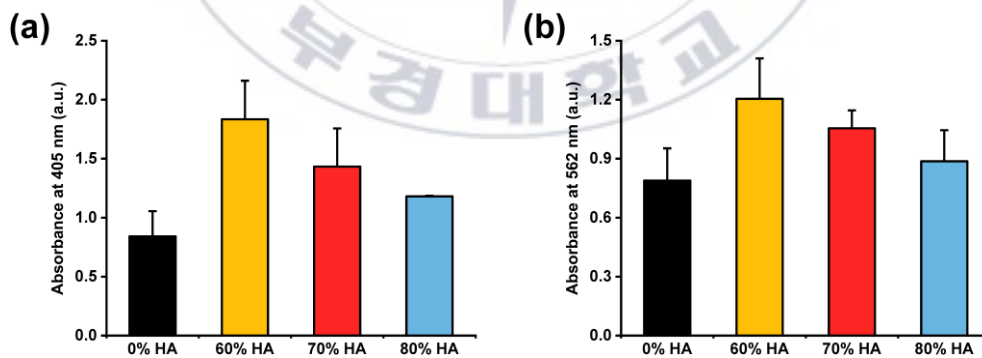


Figure 7. (a) ALP activity and (b) ARS absorbance of ADMSCs incubated on HA/gelatin composite scaffolds.

3. Optimized fabrication and characterization of 3D-printed bone scaffolds based on HA/gelatin composites reinforced with GO

In tissue engineering, the design and fabrication of scaffolds are critical for providing a proper microenvironment for cells to effectively form functional tissue [53]. Especially for the regeneration of bone tissue, a complex heterogeneous tissue with intricate hierarchical architecture, the fabricated scaffold must be precisely designed with sufficient penetration of the porous structure to meet the needs of new bone ingrowth [54]. Specifically, several researchers have reported that depending on the regeneration conditions, the ideal macropore size of a bone tissue engineering scaffold is approximately 300–900 μm with a porosity between 60% and 95% [55, 56]. However, conventional fabrication methods including particle leaching, foaming, and freeze-drying for bone tissue engineering have limitations to precisely control the overall architectures and internal pore connectivity [21]. Recently, 3D-printing technology has emerged as an innovative fabrication method and makes it possible to produce tissue-engineered scaffolds with desired external shape and controlled pore architecture [34, 57]. Moreover, its combined use with medical imaging-based 3D modeling has enabled the design and fabrication of patient-specific scaffolds with complex 3D structures [9].

As well as the pore architecture of the scaffold, the selection of biomaterials is critical and directly influences the circumstances that can lead to an effective therapeutic outcome. Among various materials, calcium phosphate-based bioceramics

including hydroxyapatite (HA) are the most commonly used for bone tissue regeneration owing to their compositional similarity to the mineral phase of natural bone tissues and excellent biocompatibility, degradability, and osteoconductivity [21, 58]. Hence, various bone substitutes have been developed and commercialized based on the major features of HA, such as promoting osseointegration and new bone formation, as well as its low toxicity [59]. However, the poor mechanical properties of pristine HA, including low fracture toughness and tensile strength, limit its potential for clinical applications, and thus researchers have focused on enhancing its intrinsic mechanical properties through the incorporation of reinforcement materials [60].

Since its rise, graphene, which is a single-atom-thick layer of sp^2 -bonded carbon atoms in a two-dimensional honeycomb lattice, has been intensively investigated as an effective reinforcement material due to its exceptional mechanical properties (Young's modulus ≈ 1 TPa, tensile strength ≈ 130 GPa, and elastic modulus ≈ 32 GPa), as well as its excellent thermal and electrical properties [61]. Furthermore, while keeping these properties to a certain extent, graphene sheets have been modified to produce various derivatives such as graphene oxide (GO) and reduced GO with widely versatile uses. In particular, GO, a highly oxidized form of chemically modified graphene, is negatively charged in an aqueous solution due to it containing hydroxyl, carboxyl, and epoxy functional groups, and thus its dispersibility is significantly improved compared with graphene [62]. In this regard, several studies have been published on the use of graphene derivatives to enhance the mechanical properties of HA as a reinforcement material. For instance, the fracture toughness and elastic modulus of pure HA were significantly enhanced by as much as 86–203% and 40–243% with GO and rGO,

respectively [63-65]. However, despite these advantages, HA-based bone scaffolds reinforced with GO via 3D-printing technology have not yet been reported. Compared to conventional fabrication methods for bone substitutes, the 3D-printing process is relatively complex, and so requires optimization to obtain precisely interconnected pore structures and appropriate mechanical properties.

Therefore, in this study, we fabricated GO-incorporated HA/gelatin composite scaffolds by using an extrusion-based 3D-printing technique with precisely designed microstructures. Gelatin, a well-known natural polymer widely used in 3D hydrogel printing, is combined with HA/GO composites to manipulate the viscosity of the ceramic slurry for proper extrusion [66]. Moreover, enhanced biomimetic properties can be provided in the HA/gelatin composite due to their synergistic advantages that mimic the inorganic and organic constituents of natural bone tissue [67]. After the preparation of the materials, the overall mechanical properties of the GO-reinforced composites were quantitatively assessed to verify the reinforcement effect before 3D-printing. Thereafter, their physicochemical and rheological properties were quantitatively analyzed and compared with controls. In addition to the assessed various properties of HA/gelatin/GO composites, their extrudability and printing resolution were precisely evaluated to optimize the parameters such as printing temperature, extrusion pressure, and printing velocity for the additive fabrication of bone scaffolds. Finally, the compressive and flexural strengths of the 3D-printed composite scaffolds fabricated with optimized printing parameters were assessed. The outcomes of the study show the feasibility of using GO-reinforced bioceramic composites for the

additive fabrication of bone scaffolds that overcome the limitations of conventional bone substitutes.



*This work has been accepted as “3D-printed hydroxyapatite/gelatin bone scaffolds reinforced with graphene oxide: optimized fabrication and mechanical characterization”. *Ceramics International*.

3.1. Materials and methods

3.1.1. Materials

Graphite powder, sulfuric acid (H_2SO_4), potassium permanganate (KMnO_4), hydrogen peroxide (H_2O_2), and type-A gelatin were purchased from Sigma Aldrich (St. Louis, USA). The hydroxyapatite (HA) powder with a particle size of less than 200 nm was purchased from nGimat, USA. All the chemicals used were of research grade.

3.1.2. The synthesis of graphene oxide

The graphene oxide (GO) was produced by the oxidation of commercially available graphite powder by using a modified Hummers method [68-70]. Briefly, graphite powder (1.0 g) was mixed in 23 mL concentrated H_2SO_4 for 2 h. Afterward, 3 g of KMnO_4 was gradually added to the mixture while keeping the temperature lower than 20 °C. The temperature was then increased to 40 °C and the mixture was stirred for 30 min. Next, the mixture was heated to 70 °C for 45 min, and 3 ml of DI water was added to the mixture followed by heating 105 °C for 5 min. Another 3 ml of DI water was added to the mixture while keeping the temperature at 105 °C for 5 min. Thereafter, 40 ml of DI water was added to the mixture while maintaining the temperature at 100 °C for 15 min. Finally, 140 ml of DI water and 3 ml of 30% H_2O_2 were added to terminate the reaction. The final solution was filtrated and washed with 10% HCl and distilled water to remove any reaction byproducts. The washed final solution was dried overnight in an oven at 40 °C.

3.1.3. Preparation of the HA/gelatin/GO composites

Composites were prepared with various concentrations of HA, gelatin, and GO, as reported in Table 1. First, synthesized GO powder was dispersed in distilled water at a concentration of 0.5% or 1% w/v via ultrasonication in a bath sonicator. Thereafter, gelatin powder was added to the GO solution at a concentration of 20% w/v and mixed using a magnetic stirrer at 70 °C for 2 h. Subsequently, 4.5, 7.5, 10.5, or 13.5 g of HA powder was added to the gelatin/GO solution followed by mixing with planetary centrifugal mixer (AR-100, Thinky Corp.) for 1 min to produce homogeneous HA/gelatin/GO composites. Specimens without GO were made by simply mixing 20% w/v gelatin solution and HA powder as a control group.

Table 2. Concentrations of the components in the HA/gelatin/GO composites.

Specimen	HA %(w/v)	Gelatin %(w/v)	GO %(w/v)	HA (g)	Gelatin (g)	GO (g)	Distilled Water (mL)
1	30	20	0	4.5	3	0	15
2	30	20	0.5	4.5	3	0.075	15
3	30	20	1	4.5	3	0.15	15
4	50	20	0	7.5	3	0	15
5	50	20	0.5	7.5	3	0.075	15
6	50	20	1	7.5	3	0.15	15
7	70	20	0	10.5	3	0	15
8	70	20	0.5	10.5	3	0.075	15
9	70	20	1	10.5	3	0.15	15
10	90	20	0	13.5	3	0	15
11	90	20	0.5	13.5	3	0.075	15
12	90	20	1	13.5	3	0.15	15

3.1.4. Characterization of HA powder, GO, and the HA/gelatin/GO composites

Morphological features were performed with a transmission electron microscope (TEM, HT-7800, Hitachi Hightech). An X-ray diffractometer (X'Pert3-Powder, PANalytical) was operated at 40 kV and 30 mA over a 2θ range of $5\text{--}80^\circ$ with $\text{CuK}\alpha$ radiation to obtain X-ray diffraction (XRD) spectra of the samples. Raman spectra of the composite scaffolds were obtained by using a micro-Raman spectrometer (NRS-5100, JASCO) with a 785 nm laser in the range $250\text{--}2500\text{ cm}^{-1}$. Fourier-transform infrared (FTIR) spectra were measured with an FT-4100 (JASCO) in the range $650\text{--}4000\text{ cm}^{-1}$. Thermogravimetric analysis (TGA) was performed by using a thermogravimetric analyzer (Pyris 1, Perkin Elmer) at a heating rate of $10\text{ }^\circ\text{C}/\text{min}$ over a temperature range of $30\text{--}800\text{ }^\circ\text{C}$.

3.1.5. Rheological measurements of the HA/gelatin/GO composites

The rheological properties of the HA/gelatin/GO composites were measured with a rheometer (HR-2, TA instruments) operating in oscillatory mode using a 20 mm parallel plate with a $1000\text{ }\mu\text{m}$ gap. To avoid dehydration, a solvent trap was used in all measurements. An amplitude sweep test was performed to confirm the linear viscoelastic region with a frequency of 1 Hz before further rheological measurements. For the temperature sweep test, the temperature was ramped up by $1\text{ }^\circ\text{C}/\text{min}$ from 15 to $50\text{ }^\circ\text{C}$ with an angular frequency of 10 rad/s and a strain of 1%. For the frequency sweep test, the angular frequency was changed 0.1 to 100 rad/s at $25\text{ }^\circ\text{C}$ with a strain of 1%.

3.1.6. 3D-printing of HA/gelatin/GO scaffold

HA/gelatin/GO composite scaffolds were fabricated by using a self-developed 3D-printing system; the overall fabrication process is summarized in Fig. 8. The prepared composites were deposited layer-by-layer through a nozzle with a diameter of 510 μm . The printing parameters including printing temperature, extrusion pressure, and printing velocity were initially set in the ranges 35–50 $^{\circ}\text{C}$, 200–500 kPa, and 1–10 mm/s, respectively, and then optimized based on the quality and accuracy of the deposited structures. The porous structures were generated while oriented at 0 $^{\circ}$ /90 $^{\circ}$ with a spacing of 1 mm and a layer height of 500 μm . The external dimensions of the scaffolds were set as a 20 \times 20 mm square shape. The strut diameters of the printed scaffolds were quantitatively assessed via optical image processing using MATLAB software.

After fabrication, the scaffolds were immersed in a solution of 0.25% w/v glutaraldehyde for 24 h at room temperature to chemically crosslink the gelatin polymeric chains. Subsequently, the scaffolds were washed three times with distilled water to remove any remaining glutaraldehyde.

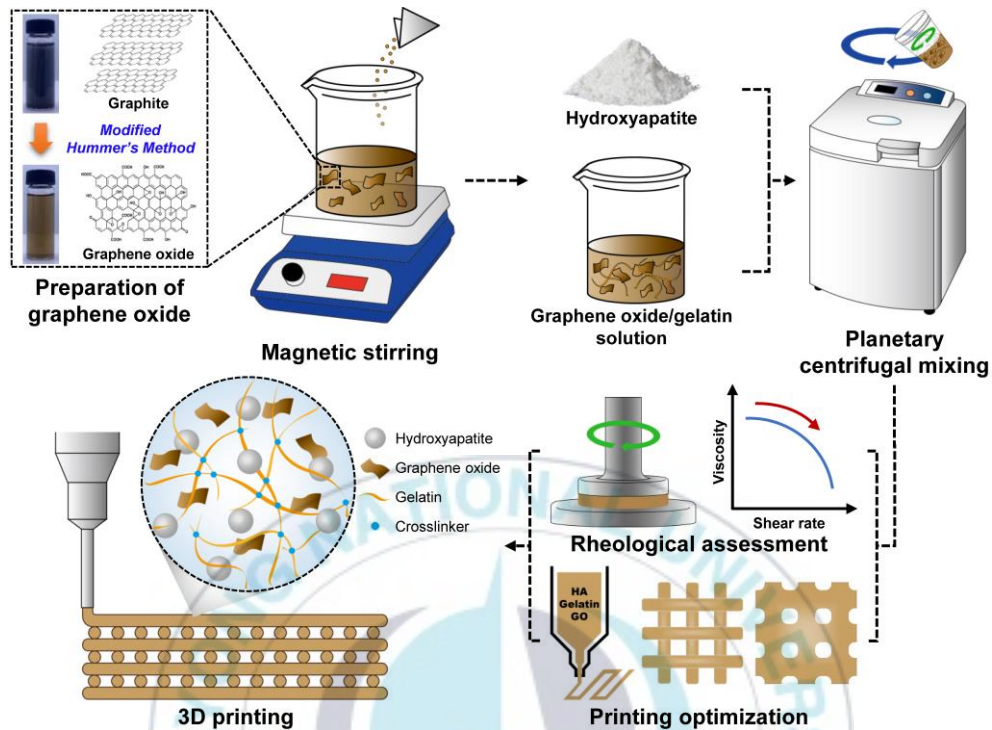


Figure 8. A schematic of the fabrication process for the 3D-printing of HA/Gelatin/GO composite scaffolds.

3.1.7. Morphological and mechanical characterization of HA/gelatin/GO scaffolds

The morphologies of the 3D-printed HA/gelatin/GO scaffolds were examined via field-emission scanning electron microscopy (MIRA 3, Tescan) after coating them with Pt. The mechanical properties of both conventionally fabricated and 3D-printed scaffolds were compared by using a universal testing machine (LR5K Plus, LLOYD Instruments).

To assess the compressive strength, cylindrical-shaped scaffolds with a diameter of 4 mm and a height of 6.5 mm are conventionally fabricated via molding and a 3D-printed 12-layer $4.5 \times 4.5 \times 4.5$ mm-sized cube-shaped scaffold were prepared and

dried at room temperature. Ten specimens from each group were tested at a constant crosshead speed of 0.5 mm/min, and the toughness of the composite scaffolds was estimated by computing the area under the stress-strain curve.

Three-point flexural testing was performed with a supporting span of 20 mm at a crosshead speed of 0.2 mm/min. The 3D-printed scaffolds (25 × 3.5 × 1.5 mm; 4 layers) were tested according to the procedure described in ASTM C1161-02c, while the flexural strength was determined as follows:

$$\sigma = \frac{3Pl}{2bd^2},$$

where P is the applied load, l is the support span distance, b is the specimen width, and d is the thickness of the specimen [71]. Twenty specimens from each group were tested to obtain an unbiased estimate of the reliability by Weibull analysis. The Weibull modulus (m) values were determined according to ASTM C1239-13 by fitting the strength data according to

$$\ln \left[\ln \left(\frac{1}{1-P_f} \right) \right] = m \left[\ln \left(\frac{\sigma}{\sigma_0} \right) \right],$$

where P_f is the probability of failure at a stress σ , and σ_0 is the characteristic flexural strength determined from the intercept of the fit to the data and m [72]. The value of σ_0 is also the stress at which the probability of failure is 63%. P_f was evaluated by applying the following relationship:

$$P_f = \frac{i-0.5}{n},$$

where n is the total number of specimens tested and i is the specimen rank numbers in ascending order of failure stress level.

3.1.8. Statistical analysis

All data are presented as the mean \pm standard deviation of independent replicates. Statistical analysis was conducted by using Student's t -tests, with *, **, and NS denoting $p < 0.05$, $p < 0.001$, and $p \geq 0.05$ (no significant difference) between groups, respectively.

3.2. Result and discussion

3.2.1. The mechanical properties of the HA/Gelatin/GO scaffolds fabricated via the conventional method

According to previous investigations, the reinforcement mechanism of graphene-based HA composites typically comes from the inhibition of crack propagation due to bridging, branching, and deflection within the composite matrix [63, 73, 74]. Furthermore, the fraction of reinforcement material within the composite matrix is an incredibly important consideration because it is an essential factor for determining the mechanical efficiency of the composites [60]. Therefore, we quantitatively assessed the mechanical properties of the HA/gelatin/GO composites with varying concentrations of blended materials to assess the reinforcement effect of GO.

As shown in Fig. 9(a), cylindrical-shaped HA/gelatin/GO scaffolds were prepared for compression testing via conventional molding with HA concentrations of 30%, 50%, 70%, or 90% and GO concentrations of 0%, 0.5%, or 1%. As can be seen in Fig. 9(b), the stress-strain curves of most of the HA/gelatin scaffolds without GO show

approximately linearly increasing stress with increasing strain followed by a sharp decline, which is the typical pattern of brittle material, except for the scaffolds with a relatively low HA ratio (30% HA/0% GO). However, the curve of the scaffolds with incorporated GO slowly dropped after the maximum strength point followed by a horizontal ductile plateau after elastic deformation (Fig. 9(c) and 9(d)). The compressive strength and Young's modulus values of the as-fabricated HA/gelatin/GO scaffolds were plotted on the vertical bar graph with respect to HA and GO concentrations (Fig. 9(e) and 9(f)) and are presented in tables with a graded color scale in Fig. 9(g) and 9(h). The experimental results indicate that the mechanical properties of HA/gelatin scaffolds can be improved by reinforcement with GO and the level of improvement is related to the concentration of HA. In particular, the 50% and 70% HA groups showed distinct increases in both compressive strength and Young's modulus values with GO incorporation. Furthermore, the maximum reinforcement effect on compressive strength and Young's modulus values was observed in the scaffold with 70% HA and 1% GO, which were respectively 54% and 38% higher than those of the scaffold without GO. Moreover, the 70% HA group showed a gradual increase in both compressive strength and Young's modulus with the addition of GO, and so an HA concentration of 70% was used in composites for further study, including the 3D-printing of the composite scaffolds.

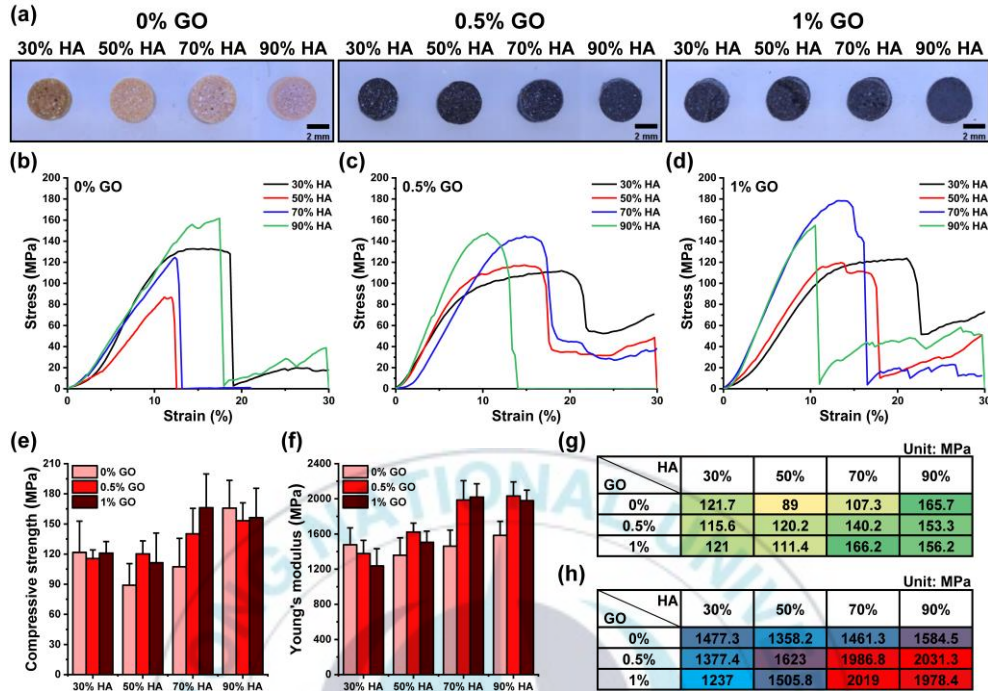


Figure 9. Compressive strength testing of conventionally fabricated HA/gelatin/GO composite cylindrical scaffolds. (a) Representative images of the fabricated HA/gelatin/GO specimens used in the compressive strength testing (scale bar = 2 mm). Stress-strain curves of HA/gelatin/GO specimens fabricated with various GO concentrations of (b) 0%, (c) 0.5%, and (d) 1%. (e) Compressive strength bar charts of the fabricated HA/gelatin/GO specimens. (f) Young's modulus plots of the fabricated HA/gelatin/GO specimens. The effect of varying the degree of GO reinforcement of HA/gelatin specimens on (g) compressive strength and (h) Young's modulus.

3.2.2. Characterization of HA powder, GO, and the HA/gelatin/GO composites

The morphology of synthesized GO was investigated by using TEM. The TEM image in Fig. 10(a) shows exfoliated GO sheets with a smooth and small wrinkled surface. UV-Vis and XPS spectra of graphite and GO were obtained to assess the degree of oxidation of GO (Fig. 10(b) and 10(c)). As expected, the UV-Vis spectrum of graphite had no remarkable absorption peaks whereas that of GO showed an absorption peak at 232 nm and a shoulder peak at 300 nm, which were attributed to $\pi-\pi^*$ transition of aromatic C=C bonds and $n-\pi^*$ transition of C=O groups, respectively [75]. The XPS spectra confirmed the existence of carbon and oxygen elements in the synthesized GO through the characteristic binding energy peaks at 285 eV and 531 eV ascribed to the C 1s and O 1s, respectively [76]. In addition, the C/O atomic ratio of the synthesized GO was measured as 1.69 using XPS, which is within the appropriate range of 1.5 to 2.5, as has been previously reported [77].

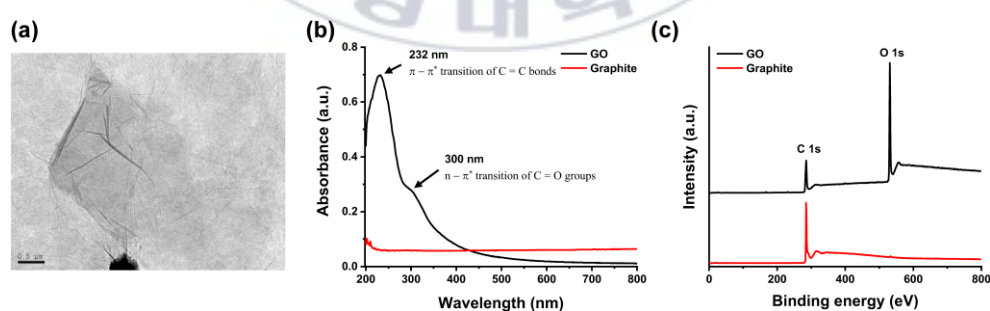


Figure 10. (a) A transmission electron microscopy (TEM) image of graphene oxide (GO), and (b) UV-Vis absorption spectra and (c) wide-scan X-ray photoelectron spectroscopy (XPS) spectra of GO and graphite.

Fig. 11(a) shows a characteristic XRD pattern of HA powder, GO, and HA/gelatin/GO composites with a GO concentration of 0, 0.5, or 1%. The XRD peaks of HA/gelatin/GO composites are consistent with the HA pattern reported in JCPDS 09-0432. Specifically, the 2θ value at 25.99° corresponds to the (002) reflection; at 28.43° to the (102) and (210) reflections; at 31.9° (triplet) to the (211), (112), and (300) reflections; and at 34° to the (202) reflection [58]. The XRD pattern of the synthesized GO presents a strong and sharp diffraction peak at $2\theta = 11.1^\circ$, which was attributed to the (002) plane. However, this peak was not detected in HA/gelatin/GO composites, most likely due to damage to their crystallographic order and the irregular arrays of atoms in three dimensions [64]. Fig. 11(b) shows FTIR spectra of HA powder, GO, and the HA/gelatin/GO composites. That of synthesized GO reveals the presence of different oxygenated functional groups: O–H stretching at $3200\text{--}3400\text{ cm}^{-1}$, C=O stretching vibrations at 1720 cm^{-1} , C–OH stretching vibrations at 1396 cm^{-1} , C–O–C epoxide groups at 1221 cm^{-1} , and C–O alkoxy groups at 1046 cm^{-1} , as well as C=C vibrations from aromatic structure domains at 1621 cm^{-1} [78]. The spectrum of HA powder shows characteristic peaks at 963 , 1016 , and 1093 cm^{-1} , which were attributed to the stretching vibration of the phosphate group [39]. The spectra of all of the HA/gelatin/GO composites presented the same characteristic peaks as the HA spectrum whereas those in the GO spectrum were overlapped by strong adsorption peaks corresponding to HA and were slightly shifted due to the characteristic groups of gelatin: the C=O stretching vibration of amide I at 1644 cm^{-1} , N–H bending of amide II at 1536 cm^{-1} , and N–H stretching of amide III at 1239 cm^{-1} .

Raman analysis was conducted to determine the existence and contribution of GO in the composites. Fig. 11(c) shows Raman spectra of HA powder, GO, and HA/gelatin/GO composites; synthesized GO is represented by typical D and G bands at around 1320 and 1574 cm^{-1} , respectively. The D band is associated with the presence of disorder in the aromatic structure or the edge effect of graphene, while the G band appeared due to the in-plane vibration of the sp^2 carbon atoms. Both of these characteristic bands of GO are also clearly evident in the spectra of the HA/gelatin/GO composites. Furthermore, the sharp peak with high intensity at 961 cm^{-1} and broad peaks at 447, 594, and 1054 cm^{-1} indicated the existence of HA in all of the composite groups. The strong peak at 961 cm^{-1} corresponds to the totally symmetric stretching mode (ν_1) of the tetrahedral PO_4 group and the relatively weak peaks at 447, 594, and 1054 cm^{-1} were attributed to the doubly degenerate bending mode (ν_2) of the PO_4 group, triply degenerate bending mode (ν_4) of the PO_4 group, and triply degenerate asymmetric stretching mode (ν_3) of the PO_4 group, respectively [79].

The thermal stabilities of HA powder, GO, and HA/gelatin/GO composites were measured from 30 to 800 $^{\circ}\text{C}$ by using TGA, the results of which are shown in Fig. 11(d). The TGA curve of GO shows characteristic thermal degradation at a temperature around 180 $^{\circ}\text{C}$, which is attributed to the pyrolysis of labile oxygen functional groups such as hydroxyl, epoxy, and carbonyl [80]. On the contrary, due to the high thermal stability of HA, the HA powder and HA/gelatin/GO composites showed relatively slow and low weight loss behavior during the heating process [81].

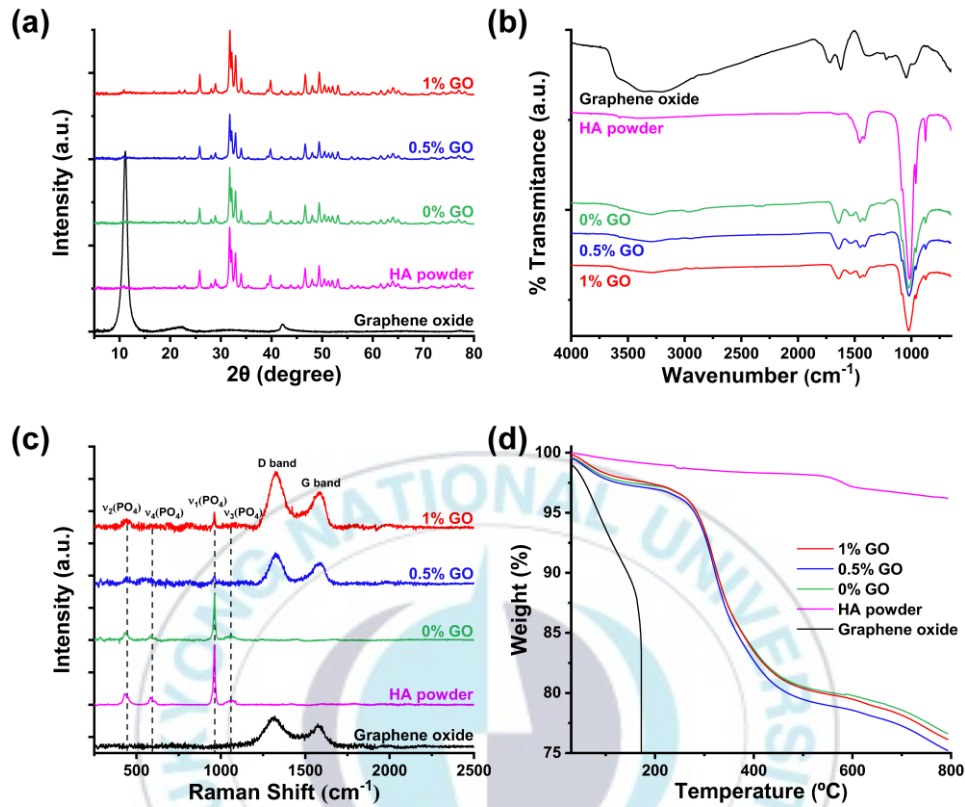


Figure 11. Characterization of HA powder, GO, and HA/gelatin/GO composites.

(a) XRD patterns, (b) FTIR spectra, (c) Raman spectra, and (d) TGA curves.

3.2.3. Rheological and printability assessments of the HA/gelatin/GO composites

To obtain 3D-printed scaffolds with precisely interconnected porous structures, the printing parameters for the HA/gelatin/GO composites were optimized based on rheological and printability assessments. Proper optimization of the printing parameters and rheological analysis of the composite is essential because each parameter, such as printing temperature, extrusion pressure, and printing velocity, is significantly affected by the rheological properties of the printing material and influences the dimensional accuracy of the fabricated scaffold [33, 82].

From the frequency sweep test (Fig. 12(a)), the storage modulus (G') was dominant over the loss modulus (G'') over the whole investigated frequency range (0.1–100 rad/s), thereby facilitating the excellent shape fidelity of the printed scaffolds [83]. In addition, both G' and G'' significantly increased with the incorporation of GO, which is favorable for maintaining the printed structure in multi-layered 3D structures [84]. Moreover, the complex viscosity of the composites was measured to confirm their shear-thinning behavior (Fig. 12(b)), which is required for their pneumatic extrusion from the nozzle; the composites with a GO concentration of 0%, 0.5%, or 1% presented distinct shear-thinning with complex viscosity that linearly decreased with increasing angular frequency. In addition to the shear-thinning behavior, the temperature-dependent rheological properties of thermo-sensitive materials such as gelatin and collagen are significant because very precise control of the temperature is required to maintain the shape fidelity of the printed scaffolds [85]. Fig. 12(c) shows temperature-dependent changes in the viscoelasticity of the composites under a temperature sweep from 15 to 50 °C. Because of the relatively high proportion of HA, there was no sol-gel transition in any of the composites below 50 °C (the crossover point between G' and G''), thereby ensuring the rheological stability of the printing material from potential phase separation during thermal change.

After analysis of the rheological properties of the HA/gelatin/GO composites, their extrudability, flow rate, and printability were examined, as presented in Fig. 12(d–h). First, the extrudability of HA/gelatin/GO composites was investigated at various printing temperatures under constant pressure and categorized into three statuses of flow rate at a fixed extrusion pressure of 500 kPa: printable (proper flow rate), non-

printable (extrudable but with an extremely low flow rate), and non-extrudable (not measurable). The results in Fig. 12(d) indicate that the composites except for the one with 1% GO were extrudable with increasing printing temperature and extruded smoothly over 45 °C. Meanwhile, the composite with 1% GO, which revealed the highest G' in the rheological assessment, needed a slightly higher printing temperature of 47.5 °C for printable extrusion. After studying the extrudability at various printing temperatures, the printing temperatures for the composites was fixed at the lowest value for each (45 °C for 0% and 0.5% GO; 47.5 °C for 1% GO) and the flow rate of the composite under varying extrusion pressure was explored (Fig. 12(e)). Seven different values of extrusion pressure from 200 to 500 kPa were applied to each group at a fixed printing temperature, and the weight of the composite material extruded for 60 seconds was measured to calculate the flow rate. The flow rate of the composite without GO was higher than those of the composites with 0.5% and 1% GO at the same printing temperature due to it having the lowest G'.

The printability of the HA/gelatin/GO composites with 0, 0.5, or 1% GO was assessed by considering the continuous extrusion and deposition of the composite materials, as shown in Fig. 12(f). Two-layered HA/gelatin/GO composite scaffolds were fabricated at varying printing velocities under a printing pressure of 350 kPa; the printing morphology and resolution were analyzed with acquired macroscopic and microscopic images of the composite scaffolds. When the composite material was extruded at higher printing speeds than the optimum (4 mm/s for 1% GO, and 10 mm/s for 0% GO and 0.5% GO), the strands of the printed scaffolds easily disconnected and the shape fidelity was poor. On the other hand, at the lowest printing speed (1 mm/s)

the pores in all the printed scaffolds were closed due to excessive localized deposition. The strut diameter of the HA/gelatin/GO scaffolds was quantitatively analyzed by using microscopic images to acquire the optimized printing parameters (Fig. 12(g-h)). The morphological images and quantified results indicate that the calculated strut diameters decreased with increasing printing velocity, while printability at a printing velocity of 7 mm/s for 0% and 0.5% GO and 3 mm/s for 1% GO was excellent with comparable strut diameters to that under ideal printing conditions (a nozzle diameter of 510 μm).



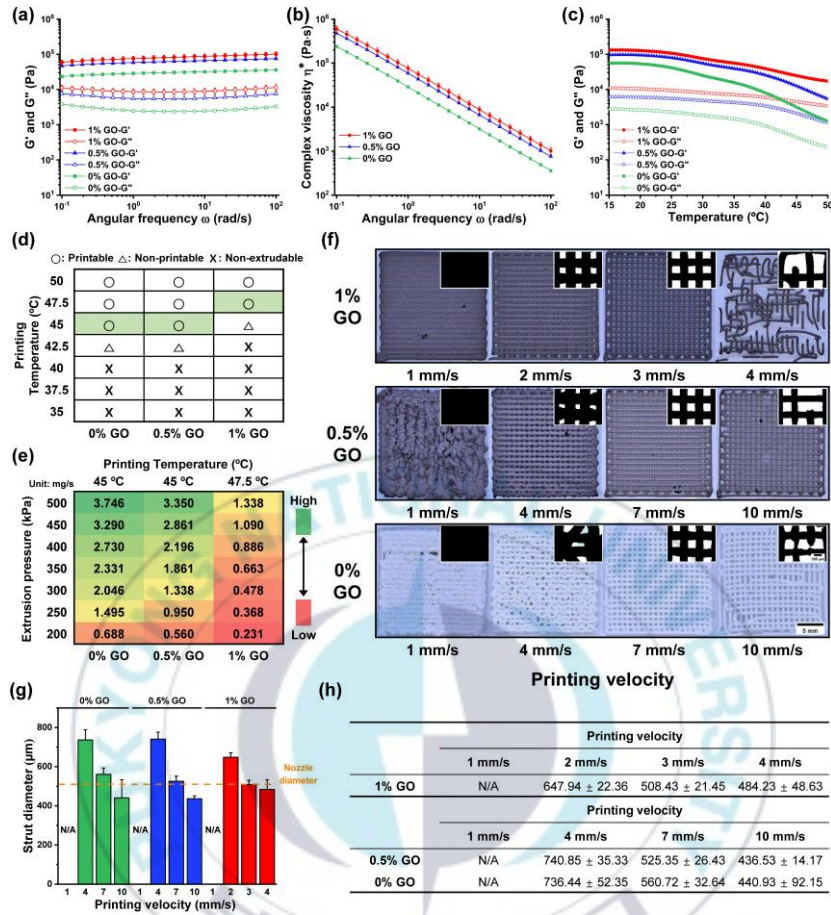


Figure 12. Rheological and printability assessments of the HA/gelatin/GO composites. (a) Oscillatory frequency sweep testing, (b) complex viscosity as a function of angular frequency, (c) oscillatory temperature ramp testing, (d) extrudability at various printing temperatures, and (e) flow rate at various extrusion pressure levels with the optimized printing temperature. (f) Representative images of the 3D-printed HA/gelatin/GO scaffolds at various printing velocities at the optimized printing temperature (scale bar = 5 mm). The inset frames are microscopy images of the 3D-printed scaffolds (scale bar = 500 μm). (g and h) Quantitatively analyzed strut diameters of the 3D-printed HA/gelatin/GO scaffolds.

3.2.4. The structural and morphological properties of 3D-printed HA/gelatin/GO composite scaffolds

Fig. 13 shows top and side view optical and SEM images of 3D-printed HA/gelatin scaffolds with varying GO concentrations (0%, 0.5%, or 1%). All of the scaffolds were stably fabricated with optimized printing parameters precisely determined via the rheological and printability assessments. As shown in the SEM images, the composite scaffolds showed a similar strut size and pore structure regardless of the varying concentrations of GO by application of the optimized printing parameters. This structural similarity is essential for avoiding unnecessary factors for mechanical assessment and accurate verification of the reinforcement effects of GO.

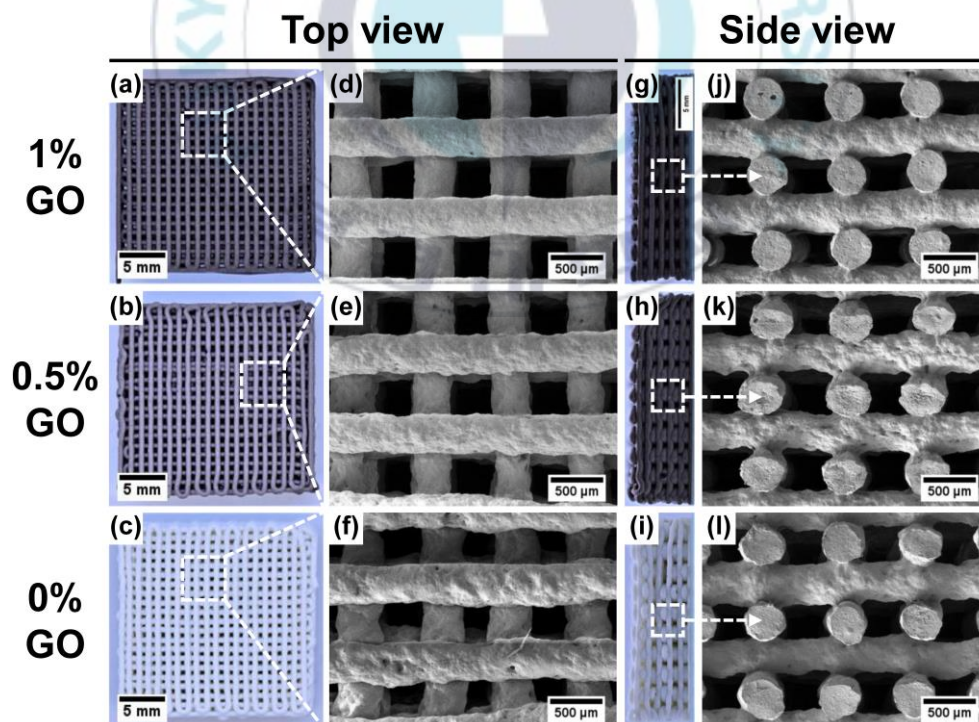


Figure 13. Morphological analysis of 3D-printed HA/gelatin/GO scaffolds. (a–c, g–i) Photographs (scale bar = 5 mm) and (d–f, j–l) SEM images (scale bar = 500 μm).

3.2.5. The mechanical properties of 3D-printed HA/gelatin/GO composite scaffolds

Compressive and three-point flexural tests were conducted to investigate the effect of GO on the mechanical properties of 3D-printed HA/gelatin/GO scaffolds. Fig. 14(a) shows representative stress-strain curves of the 3D-printed HA/gelatin/GO scaffolds with different GO concentrations under uniaxial compression. Overall, all of the scaffolds exhibited similar fracture behavior of lattice structured scaffolds without a noticeable plateau region: linear elastic behavior was observed until the ultimate strain was reached and explosive failure occurred due to multiple crack propagation within the rod segments [86]. However, the tolerance to damage (i.e., the toughness) of the HA/gelatin composite scaffolds was significantly enhanced with the proper addition of GO. Indeed, the compressive toughness of the HA/gelatin scaffold was increased by 75.7% with 0.5% GO ($676.13 \pm 165.76 \text{ kJ/m}^3$) compared to the control ($384.82 \pm 66.81 \text{ kJ/m}^3$). Fig. 14(c) and 14(d) show the compressive strength and Young's modulus values of composite scaffolds and the calculated compressive strength of all scaffolds were within the range for cancellous bone (2–12 MPa) [87]. Among them, the composite scaffolds with 0.5% GO showed the highest compressive strength of $10.28 \pm 1.08 \text{ MPa}$ and Young's modulus of $397.11 \pm 98.51 \text{ MPa}$. However, despite no significant difference between the compressive toughness of 0% GO ($384.82 \pm 66.81 \text{ kJ/m}^3$) and 1% GO ($378.54 \pm 109.76 \text{ kJ/m}^3$), the compressive strength and Young's modulus values rather decreased with the addition of 1% GO (from 8.94 ± 1.24 to $6.48 \pm 1.61 \text{ MPa}$ and 370.85 ± 46.6 to $275.97 \pm 78.46 \text{ MPa}$, respectively). This might be because relatively small and localized crosslinking in the printed filaments reduced the

reinforcement effect due to limited bridging and branching with GO while interference was increased by increased non-homogeneity. Indeed, above the optimal concentration of GO, the mechanical properties of composite scaffolds have frequently shown a decreasing trend in other studies due to the interference effect that prevents homogeneity in the composite material [88].

Fig. 14(e-h) shows three-point flexural test results with the evaluation of mechanical reliability using Weibull distribution. The estimation of mechanical reliability is critical to analyze the mechanical properties of ceramic materials, which is particularly difficult to predict fracture behaviors due to the scattered strength value [87]. To obtain an unbiased estimate of the reliability, twenty specimens for each group of HA/gelatin/GO scaffolds were fractured by applying uniaxial flexural stress. The measurements revealed relatively good fits with linear correlation coefficients of 0.93 (0% and 0.5% GO) and 0.95 (1% GO). In Fig. 14(g), the flexural strengths of all of the scaffolds were in the range of cancellous bone (10–20 MPa), although the composite with 0% GO was very near the lower limit (10.31 ± 1.84 MPa) [87]. However, the flexural strength of the HA/gelatin/GO scaffolds significantly increased by 22% with 0.5% GO (12.58 ± 2.47 MPa) and 20.3% with 1% GO (12.41 ± 1.39 MPa) compared to 0% GO (10.31 ± 1.84 MPa), which is comparable to cancellous bone. In addition, different from the compression testing of the 3D-printed scaffolds, the flexural testing revealed an increase rather than a decrease in the 1% GO sample compared to the control. When flexural testing, tensile stress is dominant over compression stress, so intrinsically tough graphene derivatives (tensile strength: 130 GPa) significantly prevent the crack propagation caused by applying tensile stress [61].

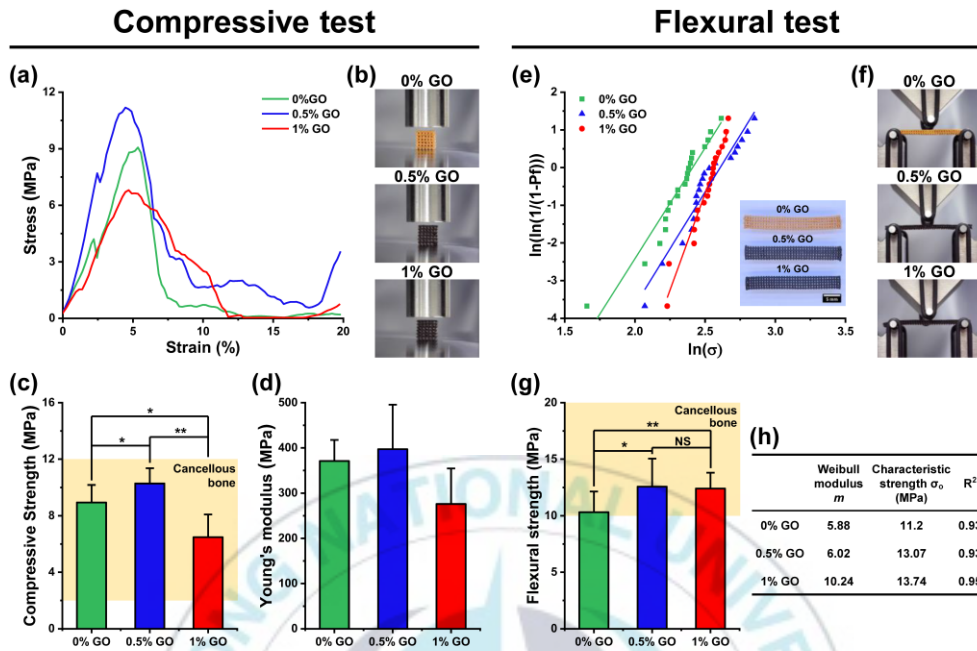


Figure 14. Compressive and flexural properties of 3D-printed HA/gelatin/GO scaffolds. (a) Stress-strain curves, (b) the testing platform for the compressive testing, (c) compressive strength, and (d) Young's modulus plots of the specimens. (e) Weibull plots to establish the flexural strengths, (f) the testing platform for the flexural testing (g) flexural strength of the specimens, and (h) Weibull modulus, characteristic strength, and correlation coefficient values of the 3D-printed scaffolds.

4. Conclusions

The work presented in this thesis focused on two different approaches to improve the applicability and functionality of HA-based composite as printing material in order to substitute conventional bone graft. Firstly, in chapter 2, biomimetic composite bone scaffolds were successfully fabricated using extrusion-based bioprinting of gelatin composites containing large weight fractions of HA (60, 70, and 80%) with the aim to provide an adequate biomimetic environment for bone tissue regeneration, with compositional and mechanical properties similar to those of the natural bone matrix. The overall features of the bioprinted HA/gelatin composite scaffolds, including rheological, morphological, physicochemical, mechanical, and biological properties, were quantitatively assessed to identify the optimal conditions for both fabrication and therapeutic efficiency. The present results show that the bioprinted bioceramic/hydrogel scaffolds possess excellent shape fidelity; mechanical strength comparable to that of native bone; and enhanced bioactivity in terms of cell proliferation, attachment, and osteogenic differentiation. These experimental findings indicate a suitable alternative direction for the bioprinting-based fabrication of bioceramic/hydrogel-based scaffolds for bone repair. Secondly, in chapter 3, GO-reinforced HA/gelatin composite scaffolds were successfully fabricated by using an extrusion-based 3D-printing technique. The overall features of the scaffolds including physicochemical, rheological, morphological, and mechanical properties were systematically evaluated. Moreover, the 3D-printing parameters were comprehensively optimized via a printability assessment to fabricate composite scaffolds with precisely controlled structures. The overall results indicate that the proper addition of GO can

efficiently reinforce the mechanical properties of HA/gelatin composite scaffolds. In particular, the compressive and flexural strength values of 3D-printed HA/gelatin scaffolds with the addition of 0.5% GO were enhanced by 15% and 22%, respectively. Moreover, the reinforcement effects of GO made the 3D-printed scaffolds compatible with cancellous bone. The outcomes of this study demonstrate the great potential of using GO to improve the mechanical properties of 3D-printed composite bone scaffolds for various applications in bone tissue engineering.



5. References

- [1] P. Wang, L. Zhao, J. Liu, M.D. Weir, X. Zhou, H.H. Xu, Bone tissue engineering via nanostructured calcium phosphate biomaterials and stem cells, *Bone research*, 2 (2014) 1-13.
- [2] T. Gong, J. Xie, J. Liao, T. Zhang, S. Lin, Y. Lin, Nanomaterials and bone regeneration, *Bone research*, 3 (2015) 1-7.
- [3] B. Ren, X. Chen, S. Du, Y. Ma, H. Chen, G. Yuan, J. Li, D. Xiong, H. Tan, Z. Ling, Injectable polysaccharide hydrogel embedded with hydroxyapatite and calcium carbonate for drug delivery and bone tissue engineering, *International journal of biological macromolecules*, 118 (2018) 1257-1266.
- [4] T. Sözen, L. Özışık, N.Ç. Başaran, An overview and management of osteoporosis, *European journal of rheumatology*, 4 (2017) 46.
- [5] H. Seitz, W. Rieder, S. Irsen, B. Leukers, C. Tille, Three-dimensional printing of porous ceramic scaffolds for bone tissue engineering, *Journal of Biomedical Materials Research Part B: Applied Biomaterials: An Official Journal of The Society for Biomaterials, The Japanese Society for Biomaterials, and The Australian Society for Biomaterials and the Korean Society for Biomaterials*, 74 (2005) 782-788.
- [6] S. Bose, S. Vahabzadeh, A. Bandyopadhyay, Bone tissue engineering using 3D printing, *Materials today*, 16 (2013) 496-504.
- [7] W. Wang, K.W. Yeung, Bone grafts and biomaterials substitutes for bone defect repair: A review, *Bioactive materials*, 2 (2017) 224-247.
- [8] J.F. Keating, A. Simpson, C. Robinson, The management of fractures with bone loss, *The Journal of bone and joint surgery. British volume*, 87 (2005) 142-150.
- [9] L. Zhang, G. Yang, B.N. Johnson, X. Jia, Three-dimensional (3D) printed scaffold and material selection for bone repair, *Acta Biomaterialia*, 84 (2019) 16-33.
- [10] I.A. Neacsu, A.P. Serban, A.I. Nicoara, R. Trusca, V.L. Ene, F. Iordache, Biomimetic composite scaffold based on naturally derived biomaterials, *Polymers*, 12 (2020) 1161.
- [11] B.D. Smith, D.A. Grande, The current state of scaffolds for musculoskeletal regenerative applications, *Nature Reviews Rheumatology*, 11 (2015) 213-222.
- [12] M. Shokouhimehr, A.S. Theus, A. Kamalakar, L. Ning, C. Cao, M.L. Tomov, J.M. Kaiser, S. Goudy, N.J. Willett, H.W. Jang, 3D Bioprinted Bacteriostatic Hyperelastic Bone Scaffold for Damage-Specific Bone Regeneration, *Polymers*, 13 (2021) 1099.
- [13] G. Brunello, S. Sivoletta, R. Meneghello, L. Ferroni, C. Gardin, A. Piattelli, B. Zavan, E. Bressan, Powder-based 3D printing for bone tissue engineering, *Biotechnology advances*, 34 (2016) 740-753.
- [14] I.T. Ozbolat, *3D Bioprinting: fundamentals, principles and applications*, Academic Press 2016.
- [15] M. Guvendiren, J. Molde, R.M. Soares, J. Kohn, *Designing biomaterials for*

- 3D printing, *ACS biomaterials science & engineering*, 2 (2016) 1679–1693.
- [16] G. Turnbull, J. Clarke, F. Picard, P. Riches, L. Jia, F. Han, B. Li, W. Shu, 3D bioactive composite scaffolds for bone tissue engineering, *Bioactive materials*, 3 (2018) 278–314.
- [17] N. Siddiqui, S. Asawa, B. Birru, R. Baadhe, S. Rao, PCL-based composite scaffold matrices for tissue engineering applications, *Molecular biotechnology*, 60 (2018) 506–532.
- [18] M. Shahrezaee, M. Salehi, S. Keshtkari, A. Oryan, A. Kamali, B. Shekarchi, In vitro and in vivo investigation of PLA/PCL scaffold coated with metformin-loaded gelatin nanocarriers in regeneration of critical-sized bone defects, *Nanomedicine: Nanotechnology, Biology and Medicine*, 14 (2018) 2061–2073.
- [19] M. Milazzo, N. Contessi Negrini, S. Scialla, B. Marelli, S. Farè, S. Danti, M.J. Buehler, Additive Manufacturing Approaches for Hydroxyapatite-Reinforced Composites, *Advanced Functional Materials*, 29 (2019) 1903055.
- [20] S. Lee, D. Choi, J.-H. Shim, W. Nam, Efficacy of three-dimensionally printed polycaprolactone/beta tricalcium phosphate scaffold on mandibular reconstruction, *Scientific reports*, 10 (2020) 1–9.
- [21] X. Du, S. Fu, Y. Zhu, 3D printing of ceramic-based scaffolds for bone tissue engineering: An overview, *Journal of Materials Chemistry B*, 6 (2018) 4397–4412.
- [22] S. Kuttappan, D. Mathew, M.B. Nair, Biomimetic composite scaffolds containing bioceramics and collagen/gelatin for bone tissue engineering—A mini review, *International journal of biological macromolecules*, 93 (2016) 1390–1401.
- [23] S. Liu, X. Wu, J. Hu, Z. Wu, Y. Zheng, Preparation and characterisation of a novel polylactic acid/hydroxyapatite/graphene oxide/aspirin drug-loaded biomimetic composite scaffold, *New Journal of Chemistry*, 45 (2021) 10788–10797.
- [24] A. Skardal, A. Atala, Biomaterials for integration with 3-D bioprinting, *Annals of biomedical engineering*, 43 (2015) 730–746.
- [25] T.-S. Jang, H.-D. Jung, H.M. Pan, W.T. Han, S. Chen, J. Song, 3D printing of hydrogel composite systems: Recent advances in technology for tissue engineering, *International Journal of Bioprinting*, 4 (2018).
- [26] R.Y. Basha, S.K. TS, M. Doble, Design of biocomposite materials for bone tissue regeneration, *Materials Science and Engineering: C*, 57 (2015) 452–463.
- [27] Y. Luo, A. Lode, A.R. Akkineni, M. Gelinsky, Concentrated gelatin/alginate composites for fabrication of predesigned scaffolds with a favorable cell response by 3D plotting, *RSC Advances*, 5 (2015) 43480–43488.
- [28] S. Chen, Y. Shi, X. Zhang, J. Ma, 3D printed hydroxyapatite composite scaffolds with enhanced mechanical properties, *Ceramics International*, 45 (2019) 10991–10996.
- [29] J. Aho, J.P. Boetker, S. Baldursdottir, J. Rantanen, Rheology as a tool for evaluation of melt processability of innovative dosage forms, *International journal of pharmaceutics*, 494 (2015) 623–642.
- [30] T. Guo, T.R. Holzberg, C.G. Lim, F. Gao, A. Gargava, J.E. Trachtenberg,

- A.G. Mikos, J.P. Fisher, 3D printing PLGA: a quantitative examination of the effects of polymer composition and printing parameters on print resolution, *Biofabrication*, 9 (2017) 024101.
- [31] B. Webb, B.J. Doyle, Parameter optimization for 3D bioprinting of hydrogels, *Bioprinting*, 8 (2017) 8-12.
- [32] Y. Zhao, Y. Li, S. Mao, W. Sun, R. Yao, The influence of printing parameters on cell survival rate and printability in microextrusion-based 3D cell printing technology, *Biofabrication*, 7 (2015).
- [33] M.H. Kim, Y.W. Lee, W.K. Jung, J. Oh, S.Y. Nam, Enhanced rheological behaviors of alginate hydrogels with carrageenan for extrusion-based bioprinting, *Journal of the Mechanical Behavior of Biomedical Materials*, 98 (2019) 187-194.
- [34] M.H. Kim, C. Yun, E.P. Chalisserry, Y.W. Lee, H.W. Kang, S.-H. Park, W.-K. Jung, J. Oh, S.Y. Nam, Quantitative analysis of the role of nanohydroxyapatite (nHA) on 3D-printed PCL/nHA composite scaffolds, *Materials Letters*, 220 (2018) 112-115.
- [35] L. Ouyang, R. Yao, Y. Zhao, W. Sun, Effect of bioink properties on printability and cell viability for 3D bioplotting of embryonic stem cells, *Biofabrication*, 8 (2016).
- [36] N. Paxton, W. Smolan, T. Böck, F. Melchels, J. Groll, T. Jungst, Proposal to assess printability of bioinks for extrusion-based bioprinting and evaluation of rheological properties governing bioprintability, *Biofabrication*, 9 (2017).
- [37] H. Wang, C. Chu, R. Cai, S. Jiang, L. Zhai, J. Lu, X. Li, S. Jiang, Synthesis and bioactivity of gelatin/multiwalled carbon nanotubes/hydroxyapatite nanofibrous scaffolds towards bone tissue engineering, *RSC Advances*, 5 (2015) 53550-53558.
- [38] M. Azami, A. Samadikuchaksaraei, S.A. Poursamar, Synthesis and characterization of a laminated hydroxyapatite/gelatin nanocomposite scaffold with controlled pore structure for bone tissue engineering, *International Journal of Artificial Organs*, 33 (2010) 86-95.
- [39] S. Salehi, M.H. Fathi, Fabrication and characterization of sol-gel derived hydroxyapatite/zirconia composite nanopowders with various yttria contents, *Ceramics International*, 36 (2010) 1659-1667.
- [40] C.S. Ki, D.H. Baek, K.D. Gang, K.H. Lee, I.C. Um, Y.H. Park, Characterization of gelatin nanofiber prepared from gelatin-formic acid solution, *Polymer*, 46 (2005) 5094-5102.
- [41] M.C. Chang, J. Tanaka, XPS study for the microstructure development of hydroxyapatite-collagen nanocomposites cross-linked using glutaraldehyde, *Biomaterials*, 23 (2002) 3879-3885.
- [42] Y. Chen, W. Lu, Y. Guo, Y. Zhu, H. Lu, Y. Wu, Superhydrophobic coatings on gelatin-based films: Fabrication, characterization and cytotoxicity studies, *RSC Advances*, 8 (2018) 23712-23719.
- [43] F.J. Martínez-Vázquez, M.V. Cabañas, J.L. Paris, D. Lozano, M. Vallet-Regí, Fabrication of novel Si-doped hydroxyapatite/gelatine scaffolds by rapid prototyping for drug delivery and bone regeneration, *Acta Biomaterialia*, 15

(2015) 200–209.

- [44] A. Samadikuchaksaraei, M. Gholipourmalekabadi, E. Erfani Ezadyar, M. Azami, M. Mozafari, B. Johari, S. Kargozar, S.B. Jameie, A. Korourian, A.M. Seifalian, Fabrication and in vivo evaluation of an osteoblast-conditioned nano-hydroxyapatite/gelatin composite scaffold for bone tissue regeneration, *Journal of Biomedical Materials Research – Part A*, 104 (2016) 2001–2010.
- [45] L.-C. Gerhardt, A.R. Boccaccini, Bioactive Glass and Glass-Ceramic Scaffolds for Bone Tissue Engineering, *Materials*, 3 (2010) 3867–3910.
- [46] J.-W. Kim, K.-H. Shin, Y.-H. Koh, M.J. Hah, J. Moon, H.-E. Kim, Production of Poly(ϵ -Caprolactone)/Hydroxyapatite Composite Scaffolds with a Tailored Macro/Micro-Porous Structure, High Mechanical Properties, and Excellent Bioactivity, *Materials*, 10 (2017) 1123.
- [47] S. Eosoly, S. Lohfeld, D. Brabazon, Effect of hydroxyapatite on biodegradable scaffolds fabricated by SLS, *Key Engineering Materials*, 2009, pp. 659–662.
- [48] Y. Xia, P.Y. Zhou, X.S. Cheng, Y. Xie, C. Liang, C. Li, S.G. Xu, Selective laser sintering fabrication of nano-hydroxyapatite/poly- ϵ -caprolactone scaffolds for bone tissue engineering applications, *International Journal of Nanomedicine*, 8 (2013) 4197–4213.
- [49] C. Isikli, V. Hasirci, N. Hasirci, Development of porous chitosan-gelatin/hydroxyapatite composite scaffolds for hard tissue-engineering applications, *Journal of Tissue Engineering and Regenerative Medicine*, 6 (2012) 135–143.
- [50] D.E. MacDonald, B.E. Rapuano, N. Deo, M. Stranick, P. Somasundaran, A.L. Boskey, Thermal and chemical modification of titanium-aluminum-vanadium implant materials: Effects on surface properties, glycoprotein adsorption, and MG63 cell attachment, *Biomaterials*, 25 (2004) 3135–3146.
- [51] D.D. Deligianni, N.D. Katsala, P.G. Koutsoukos, Y.F. Missirlis, Effect of surface roughness of hydroxyapatite on human bone marrow cell adhesion, proliferation, differentiation and detachment strength, *Biomaterials*, 22 (2000) 87–96.
- [52] T.P. Kunzler, T. Drobek, M. Schuler, N.D. Spencer, Systematic study of osteoblast and fibroblast response to roughness by means of surface-morphology gradients, *Biomaterials*, 28 (2007) 2175–2182.
- [53] D.W. Hutmacher, M. Sittinger, M.V. Risbud, Scaffold-based tissue engineering: Rationale for computer-aided design and solid free-form fabrication systems, *Trends in Biotechnology*, 22 (2004) 354–362.
- [54] L. Zhao, X. Pei, L. Jiang, C. Hu, J. Sun, F. Xing, C. Zhou, Y. Fan, X. Zhang, Bionic design and 3D printing of porous titanium alloy scaffolds for bone tissue repair, *Composites Part B: Engineering*, 162 (2019) 154–161.
- [55] K. Zhang, Y. Fan, N. Dunne, X. Li, Effect of microporosity on scaffolds for bone tissue engineering, *Regenerative Biomaterials*, 5 (2018) 115–124.
- [56] N. Arabi, A. Zamanian, S.N. Rashvand, F. Ghorbani, The Tunable Porous Structure of Gelatin-Bioglass Nanocomposite Scaffolds for Bone Tissue Engineering Applications: Physicochemical, Mechanical, and In Vitro Properties,

- Macromolecular Materials and Engineering, 303 (2018).
- [57] A.V. Do, B. Khorsand, S.M. Geary, A.K. Salem, 3D Printing of Scaffolds for Tissue Regeneration Applications, *Advanced Healthcare Materials*, 4 (2015) 1742–1762.
- [58] H. Lee, J.M. Yoo, S.Y. Nam, Additive fabrication and characterization of biomimetic composite bone scaffolds with high hydroxyapatite content, *Gels*, 7 (2021).
- [59] H.A. Siddiqui, K.L. Pickering, M.R. Mucalo, A review on the use of hydroxyapatite– carbonaceous structure composites in bone replacement materials for strengthening purposes, *Materials*, 11 (2018).
- [60] M. Li, P. Xiong, F. Yan, S. Li, C. Ren, Z. Yin, A. Li, H. Li, X. Ji, Y. Zheng, Y. Cheng, An overview of graphene-based hydroxyapatite composites for orthopedic applications, *Bioactive Materials*, 3 (2018) 1–18.
- [61] R. Geetha Bai, N. Ninan, K. Muthoosamy, S. Manickam, Graphene: A versatile platform for nanotheranostics and tissue engineering, *Progress in Materials Science*, 91 (2018) 24–69.
- [62] D.R. Dreyer, S. Park, C.W. Bielawski, R.S. Ruoff, The chemistry of graphene oxide, *Chemical Society Reviews*, 39 (2010) 228–240.
- [63] Y. Liu, J. Huang, H. Li, Synthesis of hydroxyapatite–reduced graphite oxide nanocomposites for biomedical applications: Oriented nucleation and epitaxial growth of hydroxyapatite, *Journal of Materials Chemistry B*, 1 (2013) 1826–1834.
- [64] M. Li, Y. Wang, Q. Liu, Q. Li, Y. Cheng, Y. Zheng, T. Xi, S. Wei, In situ synthesis and biocompatibility of nano hydroxyapatite on pristine and chitosan functionalized graphene oxide, *Journal of Materials Chemistry B*, 1 (2013) 475–484.
- [65] S. Baradaran, E. Moghaddam, W.J. Basirun, M. Mehrali, M. Sookhakian, M. Hamdi, M.R.N. Moghaddam, Y. Alias, Mechanical properties and biomedical applications of a nanotube hydroxyapatite–reduced graphene oxide composite, *Carbon*, 69 (2014) 32–45.
- [66] D. Kim, J. Lee, G. Kim, Biomimetic gelatin/HA biocomposites with effective elastic properties and 3D–structural flexibility using a 3D–printing process, *Additive Manufacturing*, 36 (2020).
- [67] M. Milazzo, N. Contessi Negrini, S. Scialla, B. Marelli, S. Farè, S. Danti, M.J. Buehler, Additive Manufacturing Approaches for Hydroxyapatite–Reinforced Composites, *Advanced Functional Materials*, 29 (2019).
- [68] J. Chen, B. Yao, C. Li, G. Shi, An improved Hummers method for eco-friendly synthesis of graphene oxide, *Carbon*, 64 (2013) 225–229.
- [69] K. Yang, L. Feng, H. Hong, W. Cai, Z. Liu, Preparation and functionalization of graphene nanocomposites for biomedical applications, *Nature Protocols*, 8 (2013) 2392–2403.
- [70] M.J. Yoo, H.B. Park, Effect of hydrogen peroxide on properties of graphene oxide in Hummers method, *Carbon*, 141 (2019) 515–522.
- [71] ASTM, C1161–02c, Standard Test Method for Flexural Strength of Advanced Ceramics at Ambient Temperature, ASTM International, West

Conshohocken, PA, 2002.

[72] ASTM, C1239-13, Standard Practice for Reporting Uniaxial Strength Data and Estimating Weibull Distribution Parameters for Advanced Ceramics, ASTM International, West Conshohocken, PA, 2018.

[73] L. Zhang, W. Liu, C. Yue, T. Zhang, P. Li, Z. Xing, Y. Chen, A tough graphene nanosheet/hydroxyapatite composite with improved in vitro biocompatibility, *Carbon*, 61 (2013) 105-115.

[74] Y. Zhao, K.N. Sun, W.L. Wang, Y.X. Wang, X.L. Sun, Y.J. Liang, X.N. Sun, P.F. Chui, Microstructure and anisotropic mechanical properties of graphene nanoplatelet toughened biphasic calcium phosphate composite, *Ceramics International*, 39 (2013) 7627-7634.

[75] R.A. Senthil, A. Selvi, P. Arunachalam, L.S. Amudha, J. Madhavan, A.M. Al-Mayouf, A sensitive electrochemical detection of hydroquinone using newly synthesized α -Fe₂O₃-graphene oxide nanocomposite as an electrode material, *Journal of Materials Science: Materials in Electronics*, 28 (2017) 10081-10091.

[76] K.C. Sunil, S. Suvarna, R.K. Nairy, G. Chethan, M.S. Mustak, N. Yerol, Facile, cost-effective and eco-friendly synthesis of carbonyl-rich partially reduced graphene oxide using glucose as a sole precursor, *SN Applied Sciences*, 2 (2020).

[77] M.P. Araújo, O.S.G.P. Soares, A.J.S. Fernandes, M.F.R. Pereira, C. Freire, Tuning the surface chemistry of graphene flakes: new strategies for selective oxidation, *RSC Advances*, 7 (2017) 14290-14301.

[78] C. Liu, H. Liu, A. Xu, K. Tang, Y. Huang, C. Lu, In situ reduced and assembled three-dimensional graphene aerogel for efficient dye removal, *Journal of Alloys and Compounds*, 714 (2017) 522-529.

[79] J.H. Kim, S.H. Kim, H.K. Kim, T. Akaike, S.C. Kim, Synthesis and characterization of hydroxyapatite crystals: A review study on the analytical methods, *Journal of Biomedical Materials Research*, 62 (2002) 600-612.

[80] A. Gupta, R. Jamatia, R.A. Patil, Y.R. Ma, A.K. Pal, Copper Oxide/Reduced Graphene Oxide Nanocomposite-Catalyzed Synthesis of Flavanones and Flavanones with Triazole Hybrid Molecules in One Pot: A Green and Sustainable Approach, *ACS Omega*, 3 (2018) 7288-7299.

[81] M. Li, Q. Liu, Z. Jia, X. Xu, Y. Cheng, Y. Zheng, T. Xi, S. Wei, Graphene oxide/hydroxyapatite composite coatings fabricated by electrophoretic nanotechnology for biological applications, *Carbon*, 67 (2014) 185-197.

[82] B. Joseph, J. James, Y. Grohens, N. Kalarikkal, S. Thomas, Additive Manufacturing of Poly (ϵ -Caprolactone) for Tissue Engineering, *JOM*, 72 (2020) 4127-4138.

[83] Q. Gao, X. Niu, L. Shao, L. Zhou, Z. Lin, A. Sun, J. Fu, Z. Chen, J. Hu, Y. Liu, Y. He, 3D printing of complex GelMA-based scaffolds with nanoclay, *Biofabrication*, 11 (2019).

[84] X. Yun, B. Lu, Z. Xiong, B. Jia, B. Tang, H. Mao, T. Zhang, X. Wang, Direct 3D printing of a graphene oxide hydrogel for fabrication of a high areal specific capacitance microsupercapacitor, *RSC Advances*, 9 (2019) 29384-29395.

[85] M.E. Cooke, D.H. Rosenzweig, The rheology of direct and suspended

extrusion bioprinting, *APL Bioengineering*, 5 (2021).

[86] S. Eqtesadi, A. Motealleh, R. Wendelbo, A.L. Ortiz, P. Miranda, Reinforcement with reduced graphene oxide of bioactive glass scaffolds fabricated by robocasting, *Journal of the European Ceramic Society*, 37 (2017) 3695-3704.

[87] Q. Fu, E. Saiz, M.N. Rahaman, A.P. Tomsia, Toward strong and tough glass and ceramic scaffolds for bone repair, *Advanced Functional Materials*, 23 (2013) 5461-5476.

[88] J. Liu, N. Hu, X. Liu, Y. Liu, X. Lv, L. Wei, S. Zheng, Microstructure and Mechanical Properties of Graphene Oxide-Reinforced Titanium Matrix Composites Synthesized by Hot-Pressed Sintering, *Nanoscale Research Letters*, 14 (2019).

